12-2014

INVESTIGATION OF DEFORMATION AND FAILURE MECHANISMS IN NANOINDENTATION MECHANICS

Yuzhi Xia
University of Tennessee - Knoxville, yxia6@vols.utk.edu

To the Graduate Council:

I am submitting herewith a dissertation written by Yuzhi Xia entitled "INVESTIGATION OF DEFORMATION AND FAILURE MECHANISMS IN NANOINDENTATION MECHANICS." I have examined the final electronic copy of this dissertation for form and content and recommend that it be accepted in partial fulfillment of the requirements for the degree of Doctor of Philosophy, with a major in Materials Science and Engineering.

Yanfei Gao, Major Professor

We have read this dissertation and recommend its acceptance:

Hongbin Bei, George Pharr, Timothy Truster

Accepted for the Council:
Carolyn R. Hodges

Vice Provost and Dean of the Graduate School

(Original signatures are on file with official student records.)

INVESTIGATION OF DEFORMATION AND FAILURE MECHANISMS IN NANOINDENTATION MECHANICS

A Dissertation Presented for the
Doctor of Philosophy
Degree
The University of Tennessee, Knoxville

Yuzhi Xia
December 2014

Dedication

To My Family

To Many People Who Helped and Supported Me Greatly in Last 30 Years, No Matter Where They Are Now

Acknowledgements

This dissertation would not been done without the help and support from many kind people around me. Foremost among them is my adviser, Professor Yanfei Gao. He is the best adviser I could ever image. He devoted countless time and effort that leads me to the success of my doctoral research fruitfully and timely. Also he has given me invaluable wisdom and constructive advices for my future career.

I would like to express my appreciation to my committee members, Drs. George M. Pharr, Hongbin Bei, and Timothy Truster. Dr. Hongbin Bei provided invaluable experimental data on which this thesis is based. I have learned greatly from his unique scientific perspectives. Prof. George M. Pharr partly supported my research and Prof. Timothy Truster shared his profound knowledge with me.

I also would like to particularly thank Mr. Wayne Pauly, Dr. Fay Salmon, Mr. Dave Linderman and Dr. Chaodi Li for my summer intern in 3M Company.

My friends and colleagues have been constantly supported me and believed in me, including Tianlei Li, Lili Zheng, Weidong Li, Lin Li, Chao Pu, Dr. EP George, Dr. D Catoor, Dr. H Wang, Dr. F Ren, Dr. J Lou, PE Loya, Caijun Su, Yujie Meng, Mengkun Tian, Peizhi Liu, Jingxuan Ge, Sha Ouyang, Zhicong Wang, Yi Wang, Shuangchen Tang, and many people who are not listed here.

Finally, I give my best appreciation to my parents and grandparents. No words can express my gratitude to them. This dissertation is dedicated to them.

This work is partly supported by NSF and DOE, and by the Joint Institute for Advanced Materials at the University of Tennessee.

Abstract

This dissertation further extends nanoindentation to study the initiation of plasticity in single crystals in nanoscale stressed volumes, to the instrumented tests for damage evaluation and monitoring, and to the fundamental issues in deformation and failure mechanisms in relationship to the defect evolutions.

In the first project, model Fe-Cr, Fe-Ni and Fe-Cr-Ni alloys that are the basis of many structural steels were synthesized as single crystals and characterized. The compositions investigated were Fe-15Cr, Fe-30Cr, Fe-30Ni and Fe-15Cr-15Ni (atomic percent). Several key mechanical properties were determined which will be useful in further studies of irradiation/deformation-induced defects. Incipient plasticity and slip characteristics were investigated by nanoindentation on (001) and $(\bar{1}10)$ surfaces. Finally, the effects of heterogeneous pop-in mechanisms are discussed in the context of incipient plasticity in the four different alloys.

Moreover, the pop-in event mode and pop-in excursion are investigated. In previous literature, there are two kinds of pop-in mode: a single large displacement burst and multiple successive pop-ins. The size and microstructure effect are discussed for the two modes showing that multiple successive pop-ins is more likely to be appeared in fcc crystal with a smaller indenter tip. Also an analytical model is established to predict size effect in pop-in excursion for one large pop-in mode. The effect of the dislocation nucleation mechanism is discussed for the pop-in excursion.

In the last project, the pinch-torsion test is designed to evaluate Li-ion cell safety. The failure mechanism of pinch-torsion test is examined by numerical simulations and comparisons to experimental observations. Finite element models are developed to

evaluate the deformation of the separators under both pure pinch and pinch-torsion loading conditions. It is discovered that the addition of the torsion component significantly increased the maximum principal strain, which is believed to induce the internal short circuit. It is further found that the separator failure is achieved in the early stage of torsion (within a few degree of rotation).

Table of Contents

List of Tables

List of Figures

Chapter 1 Introduction

With device miniaturization, researchers and engineers are eager to have a better understanding of the material properties at small scales which are different from those of the bulk. Nanoindentation is becoming a ubiquitous and promising measurement in understanding the nanoscale deformation phenomena due to the resolutions of indenter displacement less than several nanometers. Different from conventional indentation which measures the sizes of the impression left after unload to get the hardness[1], nanoindentation has the ability to provide the information, i.e. modulus, hardness, varies continuously with depth in the sample[2, 3]. The first demonstration was in 1977 to analyze the loading and unloading curves to measure the surface properties at the micron scale[4]. The present modern treatments start in 1975 to show how the area of contact could be measured through the load-displacement curve[5]. In 1992, Oliver and Pharr developed Oliver-Pharr method to extract the elastic modulus and hardness without the image of the hardness impression[2, 3]. For this reason, the method has become a primary technique for investigating the mechanical properties of thin films and other structure features with small size. Another method was proposed with spherical indenters by Field and Swain in 1993 [6]which proved to be equivalent to the Oliver and Pharr method[7].

1.1 Pop-in events during nanoindentation

1.1.1 Previous researches on pop-in events

In a loading-controlled test, the indentation load-displacement (*P*-*h*) curve (Fig. 1) often shows one or several pop-in events which are characterized by discrete bursts of displacement. The 1st pop-in event is widely believed to be associated with the onset of the plasticity[8-15], because the *P*-*h* curve before 1st pop-in event follows the Hertzian theory which is based on elastic analysis as shown in Fig.1.1[16]. Different materials have been investigated extensively by nanoindentation as listed in Tab.1.1 to estimate the

ideal strength of single crystal. The initiation of the first displacement burst seems to be highly stochastic. Repeating the nanoindentation test on the same sample gives a significant spread of the yield load. The distribution of the pop-in events and related theoretical strength determination from nanoindentation strongly depend on various factors, i.e. loading rate[13, 17], orientation[18], machine stiffness[19], surface preparation[20], microstructure[21, 22] and temperature[12]. For example, it is shown that the pop-in events were entirely eliminated with conventional mechanical polishing compared with regular pop-in events presented in experiments after electropolishing[20]. Also the experiments for NiAl single crystal suggested that the pop-in load highly depends on the indentation orientation[18]. In addition, the maximum shear stresses determined from the pop-in loads increase with the decreasing pre-strain[22]. For spherical indenters, the diameter of the sphere is an important length scale in the load of 1st pop-in events during nanoindentation as shown in Fig. 1.2[22]. Finally, the method to calculate the project area also has a direct influence on determining 1st pop-in stress inside the sample[23].

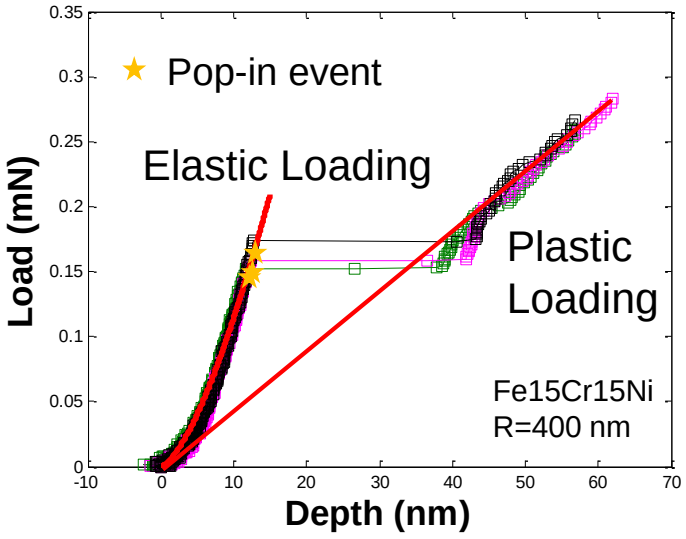

Fig. 1.1 Typical indentation curves with significant pop-in events.

Table 1.1 Recent experimental results of maximum shear stress τ_{max} inside a tested sample during nanoindentation.

Tested Sample	**Maximum Shear Stress (GPa)**	**Experimental Reference**
Pt	4.4 ($\mu/13$)	Schuh et al[12].
Al	2 ($\mu/21$)	Minor et al[24].
Ni_3Al	8 ($\mu/7$)	Wo et al[25].
Ni	8 ($\mu/7$)	Lorenz et al[26].
W	15 ($\mu/11$)	Lorenz et al[26].
SiC	25 ($\mu/7$)	Schuh and Lunh[17]
Cr_3Si	18.1-21.7 (near $\mu/7$)	Bei et al[23].
Mo-3Nb	15.4- 16.2 (near $\mu/8$)	Bei et al[14].
Ta	7.5 ($\mu/9$)	Biener et al[27].
GaN	19 ($\mu/8$)	Fujikane et al[28].
W	16.5 ($\mu/7$)	Ma et al[29].
GaAs	5-10 ($\mu/9 - \mu/17$)	Leipner et al[30].
NiAl	8.57 ($\mu/14$)	Li et al[18].
Ni	7.3 ($\mu/7$)	Wang et al[21].
Mo	16.9 ($\mu/7$)	Wang et al[21].
Mo	16.3 ($\mu/7$)	Morris et al[31].
FeCoCrNiMn alloy	4.90-5.85 (near $\mu/27$)	Zhu et al[32].
Fe-Cr-Ni alloy	2.98-7.21 ($\mu/15$)	Xia et al[33].
Cr	20.4 ($\mu/8$)	Wu and Nieh[34]

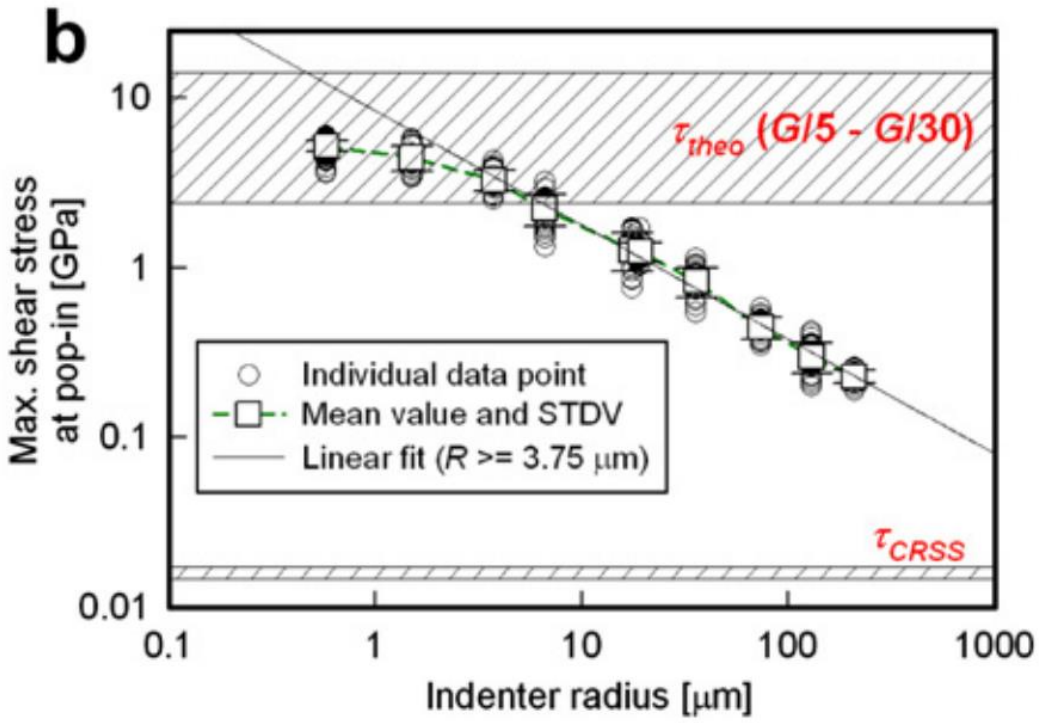

Fig. 1.2 Indentation size effect on incipient plasticity[22].

1.1.2 Homogeneous and heterogeneous dislocation nucleation mechanisms

Generally speaking, there are two kinds of dislocation nucleation mechanisms: homogenous dislocation nucleation and heterogeneous one[35]. Homogenous mechanism is that the dislocations are nucleated in crystal when the shear stress approaches the theoretical strength. In contrast, the heterogeneous dislocation nucleation mechanism is that the pre-existed defects such as vacancy concentration[13], Frank-Read source[31] and surface defects[36] serve as the heterogeneous dislocation nucleation sites to assist the process of dislocation nucleation. The heterogeneous deformation mechanism is the one commonly observed in bulk at conventional scale. The stress needed to conquer the energy barrier is much lower in heterogeneous dislocation nucleation than in homogenous one.

The viewpoint is widely accepted that the 1st pop-in event is associated with the homogenous dislocation nucleation which drives the researchers to use nanoindentation to measure the crystal strength at small volume. The first time to correlate the 1st pop-in event with the first (or first few) dislocation loop nucleation was in 1992 by Page et al[8]. They found that before the 1st pop-in event, the sample in the experiments were elastic deformed and the 1st pop-in event was the elastic-plastic transition point. This trend was also observed by idealized moledular dynamics simulation with no pre-existed defect inside[9, 11, 36-42]. In experiments, Minor first used *in situ* nanoindentation to correlate load-displacement behavior with real-time image which provides direct evidences to support the viewpoint that the 1st displacement excursion is due to homogenous dislocation nucleation during nanoindentation[24]. Additionally it was reported that homogenous dislocation nucleation may also occur when the dislocation density is $\sim 10^{14}$ m^{-2} [24].

However in some experiments, it was noticed that the pop-in load had a wider range for same sample in which some of pop-in stresses were close to the theoretical strength while some were significantly lower[12, 18, 31]. Therefore some work suggested that the heterogeneous dislocation nucleation mechanism may also be responsible for the material instability even the deformation occurs in small volume[13]. The first possible mechanism is the vacancy. Seitz showed that dislocation prefers to nucleate at a vacancy or a cluster of vacancies[43]. Furthermore, the self-diffusion of vacancy in solid may enable the formation of dislocation loop at critical radius. The activation energy for vacancy migration is relative lower (~1eV) compared with $\sim 10^{1}$-10^{2}eV for homogeneous dislocation nucleation[12, 13]. In other words, dislocation nucleation will be easier due to point defect than homogenous one from an energy viewpoint. However it is worth pointing out that the diffusion speed is low and the vacancy concentration is too low to appear in stressed volume at room temperature and at moderate pressure. Another possible mechanism is Frank-Read source, a mechanism based on dislocation multiplication in a slip plane under shear stress[44]. The multiplication of Frank-Read

source is a pure athermal, strain rate insensitive way when $\tau > \tau_c^*$ (τ_c^* is the critical resolved shear stress). The typical τ_c^* is at the order of $\sim 10^2$ MPa for which is 320MPa for Cu and 170 MPa for Al[45]. From an energy viewpoint, the activation energy is at the order of $\sim 10^0$ eV[45]. As a result, the dislocation nucleation from Frank-Read source is a promising candidate for the 1st pop-in events during nanoindention. In addition, the inclusion underneath the contact area also causes significant stress concentration and can be served as the heterogeneous sites to precede the displacement excursion which changes the shape of cumulative probability curves[13, 46]. Finally, the free surface can also be taken as the heterogeneous nucleation sites especially in thin film because atoms on the surface are weakened due to the missing neighbors[36]. The stress of surface-aided dislocation nucleation is about half of the theoretical strength in bulk. The activation energy and volume for different kinds of dislocation nucleation are summarized in Tab. 1.2.

Table 1.2 Activation energy and volume for typical dislocation nucleation mechanisms. The activation volume for homogenous dislocation nucleation is calculated as $V = r_c^3$, in which r_c is the critical radius of dislocation loop.

Dislocation nucleation type	**Activation energy ($90\%\tau_{th}$)**	**Activation volume**
Homogenous dislocation nucleation	$\sim 10^1$-10^2eV	~1-10^2b^3 [14, 47, 48]
Vacancy migration	~10^{-1}-1eV	atomic volume
Frank-Read source	~10^{-1}-1eV	10^2-10^3b^3
Surface-aided	~10^{-1}-1eV	2-30b^3

1.1.3 Current models for 1st pop-in event

In order to quantitatively investigate the dislocation nucleation behavior during nanoindentation, several statistical models were developed to predict the probabilities of 1st pop-in event or dislocation nucleation.

For homogenous dislocation nucleation mechanism, these models commonly assume that the process is rate dependent, stress-assisted and thermally activated. Thus at a given temperature the rate of homogenous dislocation nucleation obeys the Arrhenius relationship as follows

$$\dot{n} = \dot{n_0}\exp(-\frac{Q}{kT}) \tag{1-1}$$

in which $\dot{n_0}$ is an attempt frequency per material volume, Q is the activation enthalpy and kT is the thermal energy.

Schuh *et al* established the first statistical model in 2005 in which the rate is written as the form of

$$\dot{n} = \dot{n_0}\exp(-\frac{\epsilon-\sigma\Omega}{kT}) , \tag{1-2}$$

where σ is the stress over the activation volume Ω. By integrate Eq. 1-2 over the volume where the plasticity may occur, the globe rate for displacement burst is obtained as

$$\dot{N} = \dot{n_0}\exp(-\epsilon/kT)\iiint_V \exp(\frac{\sigma\Omega}{kT})dV. \tag{1-3}$$

Therefore the cumulative probability for pop-in event can be presented as[12]

$$f(t) = 1 - \exp\left(-\int_0^t \dot{N}(t')\,dt\right). \tag{1-4}$$

Eqs. 1-3 and 1-4 represent a general statistical framework for the full analysis of pop-in event during nanoindentation. Eq. 1-4 was used to fit the cumulative probability curves from experiments to obtain Ω and ϵ which are 10.2 A^3 and 0.28 eV for Pt single crystal in fitting[12]. However it is worth noting that the dislocation nucleation process is that many atoms move together to form a critical volume which implies that the volume involved in the plastic deform is much larger than the fitting value which is a typical value for one or two atoms. Also ϵ is much lower than the theoretical value of Volterra dislocation loop(~10-10^2eV)[14, 49-51]. Similar underestimation can be seen in other studies. As a result, the model proposed by Schuh is less reliable. Also Bei *et al.* used micromechanical analysis to get the theoretical value of activation energy Q and the activation volume is related to the activation energy. The predictive result shows a good agreement with the curves at high pop-in load but fails to reproduce the pop-in events at the lower load which might be caused by the heterogeneous dislocation nucleation and the uncertainty in the tip shape[14]. The model was also used in Ref.[32]. The method is mathematically complex but does not clearly shed light onto the underlying physical mechanisms. Li *et al* took the elastic anisotropy and slip systems in single crystal into consideration and presented the cumulative probability curve as follows[18]

$$f_{hom} = 1 - exp\left\langle -\dot{n}_0 \sum_\alpha \int_0^{P_{pop-in}} \iiint_\Omega \exp\left\{ -\frac{\Delta Q^{(\alpha)}\left[\tau_{RSS}^{(\alpha)}\right]}{k_B T} \right\} d\Omega \, \frac{dP}{\dot{P}} \right\rangle \qquad (1\text{-}5)$$

In order to avoid the drawback mentioned, a generally form of activation energy was used

$$Q = A\left(1 - \frac{\tau}{\tau_{th}}\right)^n \qquad (1\text{-}6)$$

in which τ is the applied shear stress and τ_{th} is the theoretical strength. A and n are obtained by fitting the cumulative probability curve which are $5Gb^3$ and 5.2 respectively. A and n fall into the value range predicted in theoretical analysis and molecular simulations which proves that this statistical model is applicable for future nanoindentation analysis of other single crystals[14, 49-54].

In some of cumulative probability curves from nanoindentation in previous literatures, significant tails at lower load can be observed which might be attributed to heterogeneous dislocation nucleation. There are several heterogeneous models that have been proposed. For vacancy migration-limit mechanism, the rate of dislocation nucleation was suggested as follows[13]

$$\dot{n} = \dot{n_0}\exp(-\frac{(Q-|\nabla\sigma_P|bV)}{kT}), \tag{1-7}$$

in which $|\nabla\sigma_P|$ is the magnitude of the pressure gradient and b is the magnitude of Burgers vector. The fitting values of activation energy and activation volume for Pt were 0.11eV and 65 A^3. This model was applied to investigate the behavior of FeCoCrNiMn alloy at different temperatures[32]. The fitting values have the same order of the one in Pt. We notice that the fitted activation energy is much smaller than the value from other measurement (1.43eV)[55] while the activation volume is slightly larger than a typical volume for point defect migration which is about an atomic volume. Furthermore, in Mason's paper, it was mentioned that the coefficient of determination R^2 is 0.36 implying that the fitting result wasn't reliable as it is expected[13]. The authors admitted that any mechanism based on vacancy diffusion is an unlikely candidate for pop-in events during nanoindentation.

Additionally a statistical model for the onset of plasticity at Frank-Read source was established to explain the size-dependence in pop-in stresses. Two assumptions were made in the model: (1) The pop-in event occurs when a pre-existing heterogeneous nucleation site is in a volume V_d where $\tau_{appl} = \tau_{defect}$. (2) The probability of finding no pre-existing defect in V_d obeys the Poisson distribution. Therefore, the cumulative probability for heterogeneous dislocation nucleation is written as follows[31]

$$f_{het} = 1 - exp\left[-\rho_{defect}V_d\right] \tag{1-8}$$

where ρ_{defect} is the pre-existing defect density in the specimen. It is interesting to note that the prediction of Morris's model only has agreement with experimental results at larger indenter radius but deviates significantly from measurement at small indenter radius.

A combined thermal-spatial statistical model was established based on homogenous and heterogeneous dislocation nucleation mechanisms[35]. The two mechanisms were treated as independent events[35]. The cumulative pop-in probability can be obtained from Eqs. 1-6 and 1-8:

$$f_{total} = 1 - exp\left\langle -\dot{n_0} \sum_{\alpha} \int_0^{P_{pop-in}} \iiint_{\Omega} \exp\left\{ -\frac{\Delta\Pi^{(\alpha)}\left[\tau_{\mathrm{RSS}}^{(\alpha)}\right]}{k_{\mathrm{B}}T} \right\} d\Omega \, \frac{dP}{\dot{P}} \right\rangle \times exp\left[-\rho_{defect} V_d\right] \quad (1-9)$$

in which the first exponential term accounts for homogenous pop-in mechanism, Eq. (5), and the second exponential term accounts for heterogeneous pop-in, Eq. 1-8. Eq. 1-9 shows excellent agreement with nanoindentation data for Mo and NiAl with different radii spherical indenters.

This unified model can be used to explain the indentation size effect on pop-in event as shown in Fig. 1.3. At small contact size, the stressed region is highly possible to be almost defect-free and pop-in event is caused by the thermal activated process of homogenous dislocation nucleation (Case A). At intermediate contact size, the probability of finding a heterogeneous dislocation nucleation site increases and there is a competition between thermally dominated statistics (homogenous dislocation nucleation) and spatially dominated statistics (heterogeneous dislocation nucleation) as shown in Case B. At larger contact size, there are a much larger number of dislocations underneath

the indenter and thus the plastic behaviors are similar with the collective plastic dynamics at continuum level (Case D).

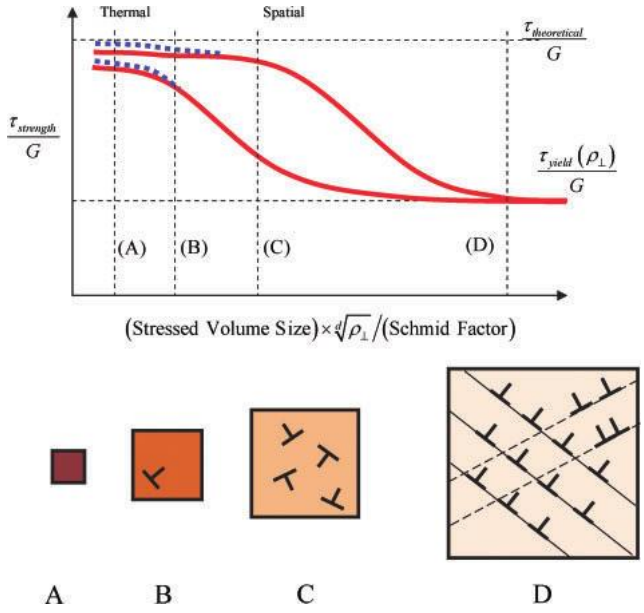

Fig. 1.3. Schematic illustration of the indentation size effect due to the stressed volume and the density of pre-existing heterogeneous sites ρ. The two red curves provide the upper and lower limits of the strength[35].

Moreover, there is another statistical model to investigate the pop-in load and maximum shear stress at 1st pop-in event in nanoindenation[56]. Similar as the unified model mentioned in last paragraph[35], two separate dislocation nucleation mechanisms were considered: nucleation of dislocations in clean crystal and activation of preexisted defect. which were treated equally. Two types of randomness were used to model the stochastic behavior. The first one is the randomness in the spatial location of preexisting defect. The other one is the randomness in the stress to activate the defect which was assumed to be uniform in Li's model[35]. The predictive results match well with the ones from recent experiments and Monte Carlo simulations.

1.2 The indentation size effect (ISE)

1.2.1 ISE in experiments

After the first several pop-ins, the nanoindentation load-displacement curves become smooth and the underlying plastic deformation transitions from stochastic behavior to continuous slip plasticity. For plastic deformation, hardness is one of the most important descriptors of the mechanical response to measure how resistant solid matter is to various kinds of permanent shape change when a force is applied. Besides the ISE on first pop-in event previous mentioned[22], another ISE in indentation is based on hardness which the contributions from both yielding and hardening are included. For example, the hardness of indentation H increases with the decrease of indentation depth h for a self-similar indenter [57, 58] and the hardness increases with the decrease of the indenter size for a spherical indenter [59], giving rise to the expression "smaller is stronger". The classical ISE experiment data came from McElhaney et al which was generated on a single crystal Cu (111) with a Berkovich indenter[60]. The data which are frequently cited demonstrates the classical ISE behavior in Fig. 1.4. Similar phenomenon has been widely observed in other investigations[61-64].

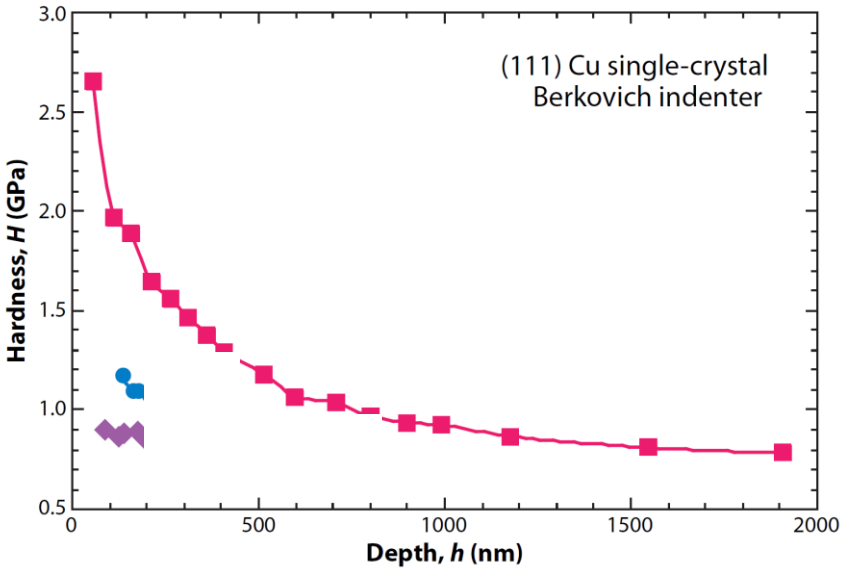

Fig. 1.4 Indentation size effect (ISE) data for (111) Cu single crystals in nanoindentation experiments. The experiments shown here were performed with a Berkovich indenter[65].

1.2.2 Nix-Gao model

Conventional theories of plasticity don't include the term of characteristic length which means that the mechanical responses from classical plasticity models are size-independent. As a result, these experiments with ISE have motivated the development of the modeling work, including strain-gradient plasticity theories based on continuum [66-75], statistical dislocation models[76-83], discrete dislocation simulation[84, 85] and other multiscale simulations[86, 87]. Most of the recent efforts to explain experimental observations have associated the size effect with the concept of geometrically necessary dislocation (GND) that is dislocations must exist to be compatible with the deformation at the contact surface [88]. Simple geometric considerations is to consider the density of GND is given as

$$\rho_G = (3\tan^2\theta)/(2bh) \tag{1-10}$$

in which θ is the centerline to face angle and b is the Burger vector for conical indenters.

At the same time, during the plastic deformation, dislocation may be generated or activated and arrested by random trapping processes, leading to the statistically stored dislocation (SSD). Based on the assumptions above and Taylor dislocation model[89], Nix and Gao developed the relation between H and h [69, 70]:

$$\left(\frac{H}{H_0}\right)^2 = 1 + \frac{h^*}{h}, \tag{1-11}$$

in which h^* is the characteristic length on the order of microns that is related to the material properties and H_0 is the indentation hardness for a large h ($h \gg h^*$). It means that the hardness is large due to the fact that the density of GND is inversely proportional to the indenter depth and appears no up bound at extreme small contact area. This model matches well with the experiment data of Cu and Ag with a Berkovich indenter [58, 60].

When it comes to spherical indentation, the ISE on hardness is a function of the radius of the sphere. Swadener et al extended the Nix-Gao's model as a function of *R* that has the similar form as Eq. 1-11:

$$\left(\frac{H}{H_0}\right)^2 = 1 + \frac{R^*}{R} \tag{1-12}$$

in which the material length scale is introduced as $R^* = \frac{\bar{r}}{b\rho_s}$, b is the burger vector and ρ_s is the density of statistically stored dislocation [59].

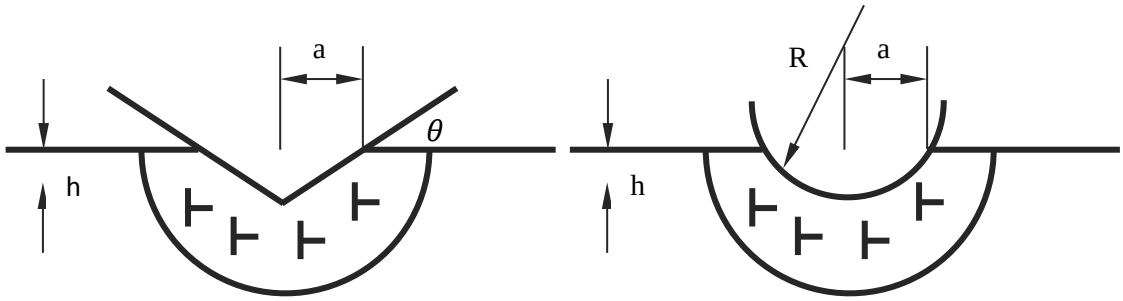

$\rho_G = 3\tan^2\theta/2bh$

$H = H_0\sqrt{1+h^*/h}$

$H_0 = 3\sqrt{3}\alpha Gb\sqrt{\rho_s}$

$h^* = 3\bar{r}\tan^2\theta/2b\rho_s$

(a)

$\rho_G = 1/bR$

$H = H_0\sqrt{1+R^*/R}$

$H_0 = 3\sqrt{3}\alpha Gb\sqrt{\rho_s}$

$h^* = \bar{r}/b\rho_s$

(b)

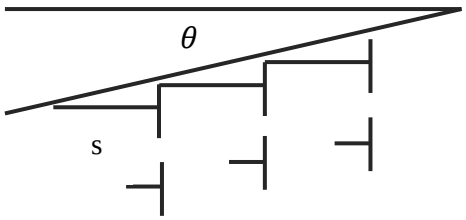

(c)

Fig. 1.5 Schematic representation of the Nix-Gao model for (a) conical indenter and (b) spherical indenter. (c) Geometrically necessary dislocation created by a rigid conical indentation. GND under a rigid spherical indenter has same representation[59].

The Nix-Gao model was incorporated into finite element model based on a CMSG (conventional mechanism-based strain gradient plasticity)[90]. The prediction shows good agreement with Ir alloy's experimental result with the exception of the smallest indenter, $R = 14\,\mu m$. At smallest radius, the theoretical prediction deviates significantly with the curve from the experiments.

Although it was widely applied and showed great predictive capabilities, the Nix-Gao model clearly overestimates the indentation hardness for very small indenters compared with a lot of experimental data from different research groups as shown in Fig. 1.6 [59, 74, 91]. At micro hardness, the H^2-$1/h$ data presents a linear behavior while the linear one deviates significantly at nano-hardness regime. The mechanism of the break-down observed is still unclear. The reason may be an experiment artifact[63, 92] or the spreading of the GNDs to a larger volume [63, 93] or dislocation source-limited behavior [94-96]. One approach to address this is that, as Huang *et al.* suggested that there is a maximum allowable density ρ_{GND}^{max} existing, due to the strong repulsive force between the dislocations that push dislocations outside the high stress volume, in order to regularize the discrepancy[74]. ρ_{GND}^{max} can be measured from experiments and is to be shown that it is on the order of 10^{-16} or 10^{-17}m^{-2}. These theories, however, do not address the exact details of dislocation microstructure formed during small-scale contact. Another way to modify Nix-Gao model is to redefine the GND volume. In original Nix-Gao model, the radius of the hemispherical zone with GNDs is equal to the radius of the contact impression. However, in small GND volume and a larger GND density, the repulsive forces tend to drive them outward to occupy a larger volume[59]. Durst et al suggested the radius scales with the contact radius by a material dependent factor f. Based on experiments and finite element method simulations, the value of f is in the range of 1.5 to 2.5 which shows well agreement with the experiments. Finally another possible reason for the deviation is the limited number of dislocation sources, a kind of model that attributes the break-down to a lack of dislocation sources when the stressed volume is small which will be discussed later.

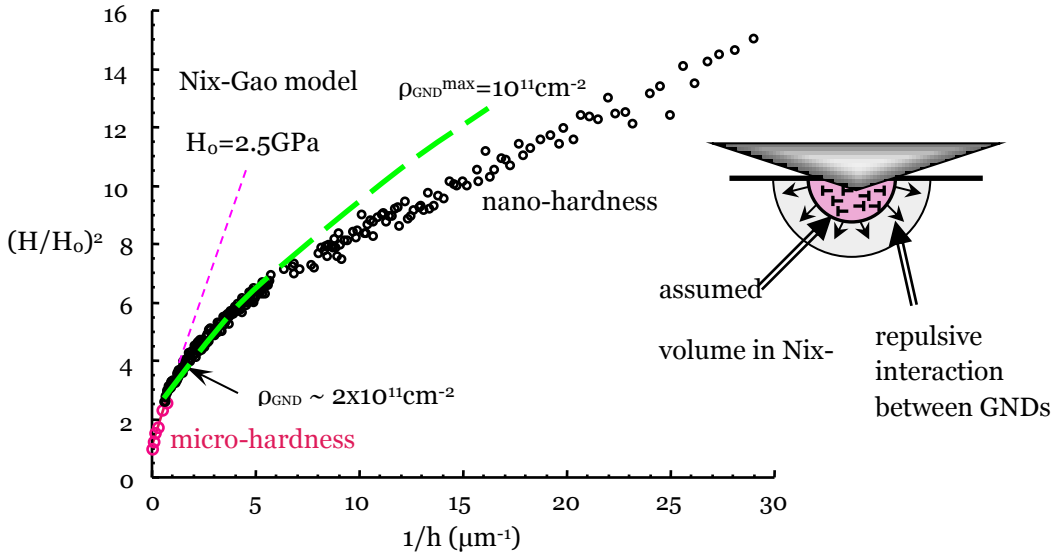

Fig. 1.6 Indentation hardness H as a function of indentation depth h for the Berkovich indentation on iridium crystals. The size dependence is often interpreted by the extra hardening due to the geometrically necessary dislocaitons (GND)[68, 73, 74]

1.2.3 Influence of dislocation source number on ISE

Some researchers suggested that ISE in strength are due to unique deformation that can be observed only when the specimen volume approaches the average dislocation spacing and thus plastic deformation is controlled by a limited number of dislocation sources. Some experiments show some evidences for the dislocation source-limited model[95, 96]. The geometry self-similarity is not obeyed in the development of GND structure and the behavior may lead to the ISE. Dislocation dynamics (DD) simulation is an effective way to provide important clues to investigate the dependence of ISE on source number, as well as the dislocation forming details [97-99]. In DD simulation, dislocations can be either randomly placed in the initial microstructure or created by the activation of dislocation sources. For example, Kreuzer and Pippan conducted 2D simulation for the activity of edge dislocation with wedge indentation and demonstrated

that the dislocation nucleation is largely due to source limited [97]. In the simulation, the result shows no ISE essentially, however, when discrete dislocation sources were added to the starting configuration, a strong ISE is observed. Recently, a detailed and thorough comparison between dislocation dynamics and crystal plasticity was made to investigate ISE [100]. Crystal plasticity simulations successfully reproduced the experimental findings at larger indentation depth. At the same time, dislocation dynamics can only capture the sectors found experimentally when there is a high obstacle density and large obstacle strength. The simulation result from DD depends largely on source density and only minorly on obstacle density. However, 2D DD simulation should be treated as an effective way to check the controlling mechanisms rather than as quantitatively prediction because of the dimension limitations [65].

1.2.4 The link between the pop-in and ISE

The goal of our research is to investigate ISE in transition from microscale to nanoscale which might be due to a breakdown of the kinematic relationship between strain gradients and GND density (e.g., a source-limited behavior). For very small indentation sizes/depths, it is necessary to consider the conditions for 1st pop-in event. Dislocation nucleation is observed in the *P-h* curve as a pop-in event, once the resolved shear stress reaches a critical value given by either homogenous strength or defect activation stress by heterogonous pop-in mechanism. After first pop-in or several pop-in events, the material is thus forced to develop a certain dislocation density which we consider the indentation force is given as

$$F = AH(\rho) \tag{1-13}$$

in which *A* is the contact area and *H* is the hardness of material. As show in Fig. 1.6, Eq. 1-13 has a linear relationship between the indentation force and the depth for spherical indenter.

During the pop-in event, the load is a constant while there is a displacement excursion. Sometimes there are several pop-ins in a *P-h* curve. They will produce a totally error in hardness measurement as shown in Fig. 1.7. Considering pop-in behavior is stochastic, the depth of measurement in ISE should be larger than the possible pop-in depth which means that the hardness should be measured in the continuous slip plasticity stage. Wang et al. checked the curves on silica polished or electropolished Ni and found that pop-in occurs at depths less than 50 nm[101]. Also Durst et al. plotted the relationship between the hardness and depth for W showing that 50 nm is a reasonable cutoff radius[102].

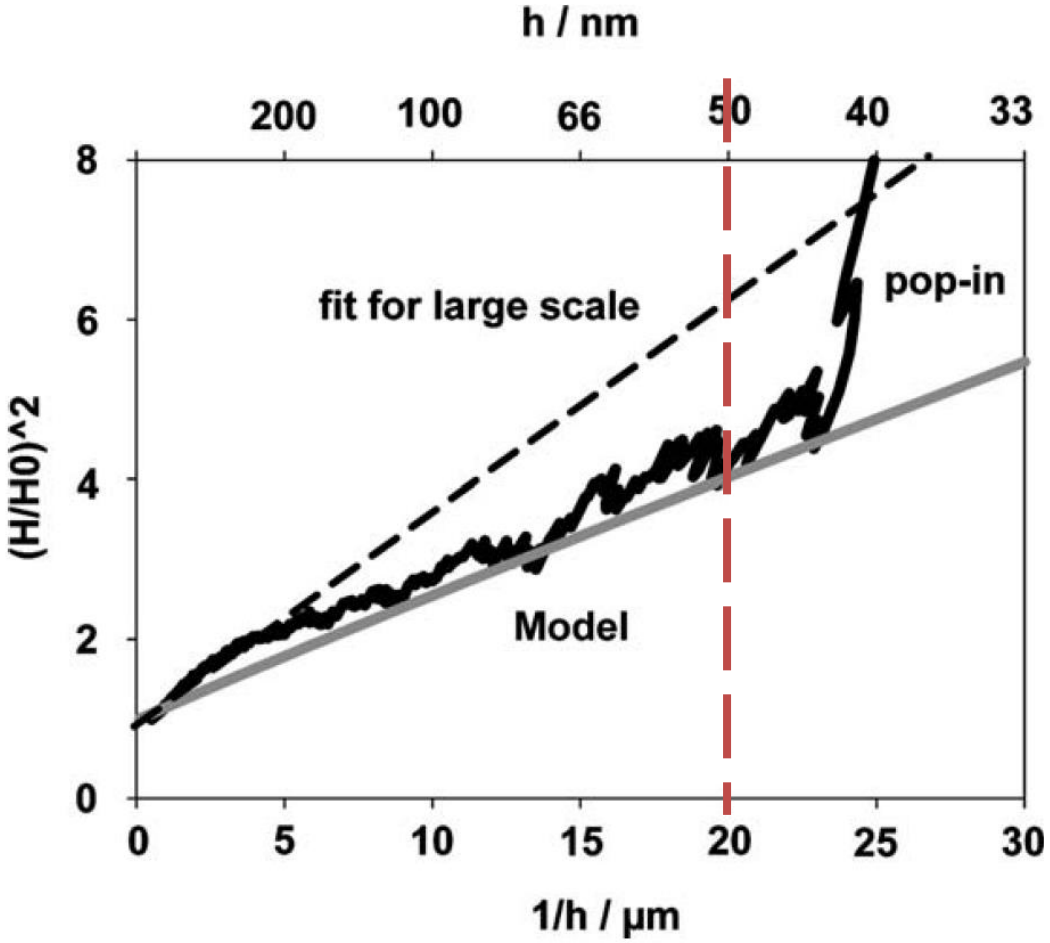

Fig. 1.7 The hardness measured as a function of the indentation depth[102].

Chapter 2 Synthesis, characterization, and nanoindentation response of single crystal Fe-Cr-Ni alloys with FCC and BCC structures

2.1 Introduction

Fe-based alloys have wide application in the nuclear industry, as structural materials in fusion nuclear reactors [103]and spallation targets in accelerator driven systems [104]. Binary Fe-Cr alloys are of interest because nuclear transmutation of these elements does not occur when irradiated with neutrons [105]. Ternary Fe-Cr-Ni alloys exhibit void swelling at much higher doses than pure metals such as iron [106]. Nevertheless, they undergo microstructural changes in extremely harsh environments that are responsible for swelling [107, 108], accelerated creep [109], and a smooth transition from elastic to plastic deformation with increased yield stress [105, 110]. To extend service lifetimes and mitigate radiation damage, a fundamental and complete understanding of defect formation and evolution at the nanoscale is necessary combined with an understanding of how they affect the macroscopic mechanical properties that govern component performance and reliability. In the past several decades, extensive experimental and theoretical research has been conducted to investigate mechanical properties and understand the underlying mechanisms [108-114]. Previous research was focused on commercial steel or specific Fe-Cr alloys. Recently, spherical indentation on polycrystalline Fe-12Cr alloy showed that initial yield occurs at a higher stress with a smoother transition from the elastic regime due to irradiation-induced defects [105]. However, relatively little is known about the complex deformation behavior under indentation in alloys with different chemistries. A basic and thorough assessment of Fe-Cr-Ni single crystals with different chemical compositions under nanoindentation will provide key information on mechanical properties at small length scales, especially the transition from incipient plasticity to continuum slip plasticity.

Instrumented nanoindentation is a powerful tool to characterize mechanical behavior at small scales [2, 3]. It measures the indentation load P and the indenter

displacement h, which allows the extraction of material properties, including modulus E and hardness H [2, 3]. Continuous stiffness measurement is usually employed with a small, sinusoidally varying load for continuous measurement of modulus E and hardness H as a function of depth. The results are influenced by indenter geometry [23], indentation orientation [18], near-surface damage [20] and pre-existing defects [31].

Nanoindentation has also been used to investigate incipient plasticity in various crystalline materials[10, 12, 14, 18, 20, 23, 31, 33]. Incipient plasticity is associated with a sudden displacement burst, or "pop-in" event, on an otherwise continuous load-displacement curve. The first "pop-in" event often denotes dislocation nucleation in materials with low dislocation density when the resolved shear stress reaches a critical value in the range of $\mu/30 - \mu/5$ where μ is the shear modulus. It is very close to the theoretical strength τ_{th} obtained from *ab initio* calculations [115]. Unlike in uniaxial loading, where it is easy to obtain the resolved shear stress [116], the stress field is much more complex during indentation. Li *et al*. [18] developed a general solution for the stress field in anisotropic Hertzian contact, which can be used to obtain the maximum resolved shear stress for any given crystallographic loading direction. The theoretically predicted orientation dependence of pop-in loads agrees well with the experiment results, consistent with the view that the first displacement burst during nanoindentation is the result of homogenous dislocation nucleation in a metal with low enough dislocation density. For a given dislocation density, the likelihood of finding a pre-existing defect that can be activated at a stress lower than the homogeneous nucleation stress increases as the volume of stressed material under the indenter increases. When that happens, the governing mechanism responsible for triggering the first pop-in event transitions from homogeneous dislocation nucleation to alternative heterogeneous mechanisms such as the sudden motion of pre-existing dislocations. Statistical models have been developed for heterogeneous pop-ins during nanoindentation to explain size-dependent pop-in stresses, in which the spatial statistics derive from the probability of finding a pre-existing defect in the stressed volume [31]. Consequently, pop-in measurements can provide not only the

theoretical strength of materials but also shed light on the density and strength of pre-existing defects that are formed during synthesis or prior deformation.

After the first several pop-ins, the nanoindentation load-displacement curves become smooth, and the underlying plastic deformation transitions from stochastic behavior to continuous slip plasticity. A number of studies using transmission electron microscopy (TEM) have been conducted to characterize dislocation patterns inside crystalline materials during this transition, including in Mg [117] and α-Ti [118]. An alternative and less tedious method by which the underlying deformation mechanisms can be inferred is surface slip trace analysis, which has been used extensively in uniaxial tests [119-122] where the intersection line between the slip plane of the activated slip systems and the specimen surface can be easily observed and analyzed. A similar approach can, in principle, be applied to the slip traces visible on indentation surfaces, which also depend only on the activated slip system and indentation direction. However, the complex stress states under the indenter makes this type of analysis considerably more difficult than in the uniaxial case and is therefore not widely used.

In this work, key mechanical properties of Fe-Cr, Fe-Ni and Fe-Cr-Ni alloys, including modulus, hardness, theoretical strength, defect density and slip systems, are investigated using ultrasonic technique, nanoindentation and slip trace analysis. The experiment results are used to analyze the deformation mechanisms, via a geometric construction, an elastic contact stress analysis, and a crystal plasticity finite element method.

2.2 Material and methods

2.2.1 Single crystal growth and sample preparation

Single crystals of Fe-15Cr, Fe-30Cr, Fe-15Cr-15Ni and Fe-30Ni (at.%) were grown in an optical floating zone furnace from polycrystalline rods produced by arc melting pure Fe, Ni and/or Cr followed by drop casting into a copper mold under Ar atmosphere. During single crystal growth, the diameter of the molten zone was carefully reduced to produce a neck that prevented the slower growing grains from propagating [123]. X-ray diffraction [Fig. 2.1(a)] confirmed that Fe-15Ni-15Cr and Fe-30Ni have the face centered cubic (FCC) structure and Fe-15Cr and Fe-30Cr have the body centered cubic (BCC) structure. Figure 2.1(b) shows an example of the as-grown Fe-15Cr single crystal. The quality and orientation of all four crystals was examined by using backscatter Laue diffraction, as shown in Fig. 2.1(c), which confirms the single crystal nature for all four alloys. Laue diffraction indicated the growth direction of Fe-15Cr, Fe-30Cr, Fe-15Cr-15Ni and Fe-30Ni are [122], [112], [012] and [112], respectively. The as-grown crystals were re-oriented using backscatter Laue diffraction and cut normal to the [100] and [110] directions using an electro-discharge machine.

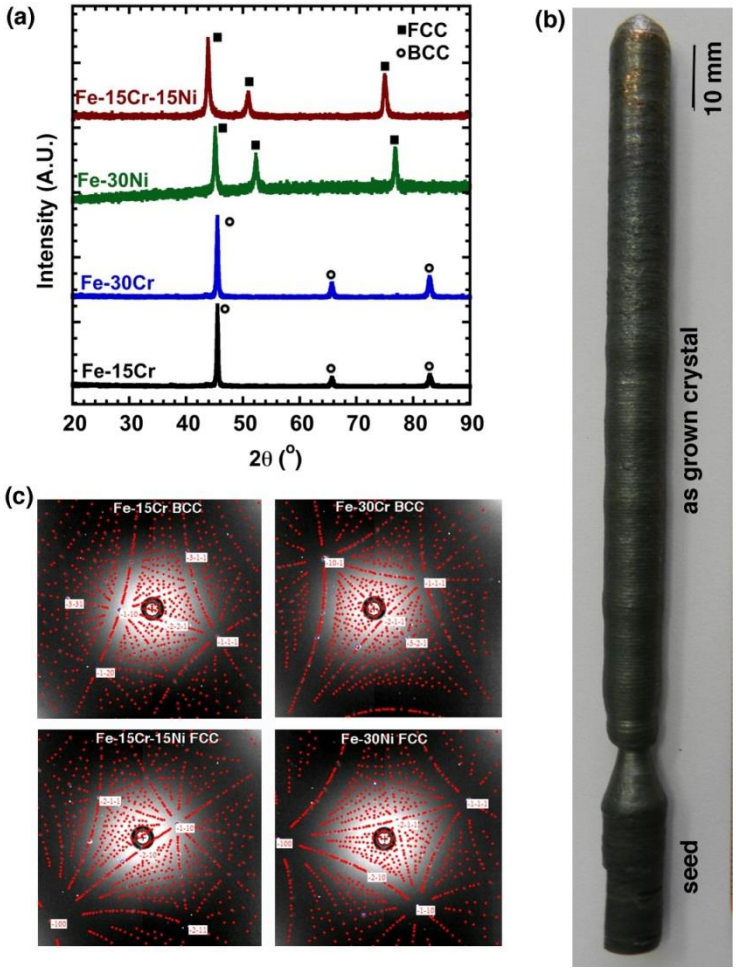

Fig. 2.1 (a) X-ray diffraction shows that Fe-15Ni-15Cr and Fe-30Ni have the face centered cubic (FCC) structure and Fe-15Cr and Fe-30Cr have the body centered cubic (BCC) structure. (b) Photograph shows an example of as-grown Fe-15Cr single crystal specimen. (c) Indexed backscatter Laue diffraction patterns showing the growth direction of the as-grown Fe-15Cr, Fe-30Cr, Fe-15Cr-15Ni and Fe-30Ni single crystals.

2.2.2 Ultrasonic method for elastic constants

The elastic constants of the two FCC crystals (Fe-30Ni and Fe-15Cr-15Ni), have been reported before [124, 125]. Therefore, here we report only the elastic constants of the two BCC single crystals obtained using the ultrasonic technique. Cylindrical rods with diameters of 6-7 mm and thickness of ~5 mm were machined and ground for this

propose. A cubic crystal has three independent elastic constants (c_{11}, c_{12} and c_{44}). Therefore, two differently oriented single crystals are needed to obtain these elastic constants. The longitudinal and transverse sound velocities for the two orientations are given by the following equations.

For the <100> crystallographic direction,

$$V_l = \left(\frac{c_{11}}{\rho}\right)^{0.5} \text{(longitudinal)}, \tag{2-1}$$

$$V_t = \left(\frac{c_{44}}{\rho}\right)^{0.5} \text{(transverse)}, \tag{2-2}$$

For the <110> direction,

$$V_l = \left(\frac{c_{11}+c_{12}+2c_{44}}{2\rho}\right)^{0.5} \text{(longitudinal)}, \tag{2-3}$$

where ρ is the specimen density, which we measured with an AccuPyc^{TM} 1330 pycnometer. The above procedure is similar to that reported in Ref. [123] where additional details can be obtained.

2.2.3 Nanoindentation and Microindentation

Samples were mounted in epoxy and metallographically prepared by grinding and polishing. To eliminate the damaged layer after mechanical polishing [20], the samples were electrochemically polished in a 85% H_3PO_4 solution with applied DC voltage of ~10 V. Three different kinds of indentation tests were conducted with a Nanoindenter-XP system (formerly MTS and presently Agilent Technologies, Oak Ridge, TN) as discussed below.

First, a Berkovich indenter was used to measure hardness and modulus using the continuous stiffness method [2, 3]. The tip area function was calibrated with a fused silica sample [2]. For diamond indenters, the Young's modulus E_i is 1141GPa and Poisson's ratio ν_i is 0.07. The measurements were performed in the continuous stiffness mode (CSM) with a constant $\dot{P}/P = 0.05\ s^{-1}$ upto a prescribed maximum load of 15 mN, which results in the maximum depth of ~ 650 nm.

Second, nanoindentation was performed along <001> using a spherical diamond indenter with a tip radius of ~400 nm to investigate pop-in events. The machine was programmed to apply a maximum load of 1 mN and the loads corresponding to the first pop-in event were recorded as the pop-in loads, P_{pop-in}. In order to investigate the statistical behaviors of specimens during nanoindentation, more than 100 indents were made on each specimen, and these indents were placed far enough from one another to avoid interference.

Third, microindentation was performed on (001) and $(\bar{1}10)$ surfaces using a spherical sapphire indenter with a radius of ~100 μm. The purpose of this test was to generate surface slip traces that could be imaged with an optical microscope to determine the active slip systems. The maximum indentation depth was 2 μm.

2.3. Results

2.3.1 Modulus and Hardness

Hardness and modulus were measured along [001] direction, and the results are summarized in Table 1. The two FCC alloys (Fe-15Cr-15Ni and Fe-30Ni) have almost identical hardness values (1.46 and 1.43 GPa, respectively). One of the BCC alloys (Fe-15Cr) has a hardness (1.65 GPa) that is similar to that of the FCC alloys, but the hardness

of the second BCC alloy, Fe-30Cr, is almost twice as high as the others (3.06 GPa). These results indicate different solid solution hardening effects in the two crystal structures. Two major reasons for solid solution hardening are atomic size mismatch and modulus mismatch [126]. In the present alloys, the atomic radii of Fe (126pm), Cr (128pm) and Ni (124pm) [127]are all very close, thus the influence of atomic size mismatch may be insignificant. On the other hand, the shear modulus of Cr is about one and a half times that of Fe or Ni [128]. Solute atoms with different moduli than the surrounding matrix change the strain field and affect dislocation motion. Therefore, the addition of Cr to Fe is expected to cause more hardening than the addition of Ni, which is consistent with the measured hardness trends in Table 2.1.

Table 2.1 Reduced modulus E^* and hardness H for the four investigated alloys.

	$\boldsymbol{E^*}$ from Oliver-Pharr method (GPa)	$\boldsymbol{E^*}$ from ultrasonic measurement (GPa)	$\boldsymbol{H}$ (GPa)
Fe-15Cr	181±9	187.4	1.65±0.03
Fe-30Cr	193±8	195.7	3.06±0.04
Fe-15Cr-15Ni	156±11	171.0	1.46±0.02
Fe-30Ni	136±7	137.3	1.43±0.02

The reduced modulus E^* was extracted from the unloading curve using continuous stiffness method [2, 3]and the results are summarized in Table 1 along with values calculated from ultrasonic wave velocity measurements as discussed below. Although nanoindentation gives reasonably good values for the reduced modulus, for elastically anisotropic materials, it is a complicated process to obtain the independent elastic constants from the nanoindentation moduli. Therefore, the ultrasonic technique

was used to obtain the elastic constants of the two BCC single crystals in this study. For the FCC single crystals, the elastic constants were taken from ref. [124, 125]. The results for the four alloys are listed in Table 2, along with the elastic anisotropy parameter $A = (2c_{44})/(c_{11} - c_{12})$ (which is unity when the material is isotropic). Fe-30Ni has the highest elastic anisotropy with $A = 3.91$ while Fe-30Cr has the lowest anisotropy with $A = 1.90$.

Table 2.2 Elastic constants (from ultrasonic measurement) and elastic anisotropy parameter *A* for the four investigated alloys.

	$\boldsymbol{c_{11}}$ (GPa)	$\boldsymbol{c_{12}}$ (GPa)	$\boldsymbol{c_{44}}$ (GPa)	$\boldsymbol{A}$
Fe-15Cr	234	128	121	2.28
Fe-30Cr	245	120	119	1.90
Fe-15Cr-15Ni [124]	211	137	130	3.51
Fe-30Ni [125]	147	89	114	3.91

Once all the independent elastic constants are available, the reduced modulus can be calculated and compared to the nanoindentation results. In nanoindentation, E^* for elastically anisotropic specimens can be calculated as follows [129]:

$$E^* = \left[1/E_{eff} + (1 - \nu_i^2)/E_i\right]^{-1} \tag{2-4}$$

where E_{eff} is the effective indentation modulus of the anisotropic specimen, and E_i and ν_i are the elastic modulus and Poisson's ratio of the indenter. E_{eff} can be obtained following the analytical procedure in Ref. [129] that solves the Hertzian contact problem of elastic anisotropic half-spaces. Clearly, it depends on the three elastic constants of these cubic crystals, as well as the crystallographic orientation of the indented surfaces. The elastic constants in Table 2.2 were used to calculate the reduced moduli E^*, which are listed in Table 1 next to the measured values from nanoindentation. The measured and calculated values of E^* for the four alloys match well (within 10%).

For comparison with our alloys, Eq. (2-4) was used to calculate the effective indentation modulus for indentation on the (001) surfaces of the pure metals iron, nickel and chromium. We obtain values of $E_{eff\_Fe} = 217$ GPa, $E_{eff\_Cr} = 294$ GPa and $E_{eff_Ni} = 203$GPa. The elastic constants used for these calculations were $c_{11} = 237$GPa, $c_{12} = 141$ GPa and $c_{44} = 116$ GPa for Fe [130], $c_{11} = 340$ GPa, $c_{12} = 59$ GPa and $c_{44} = 99$GPa for Cr [131] and $c_{11} = 244$GPa, $c_{12} = 158$GPa and $c_{44} = 102$GPa for Ni [131]. From these values of E_{eff}, the corresponding reduced moduli, E^*, for indentation with diamond can then be calculated, which are 182.5GPa, 234GPa and 172GPa for Fe, Cr and Ni, respectively. When compared to pure iron, Fe-15Cr and Fe-30Cr have higher E^*, but they lie in the range from the E^* of Fe (lower limit) to that of Cr (upper limit), indicating a normal rule-of-mixtures type behavior. In contrast, the E^* of Fe-30Ni is lower than that of *both* Ni and Fe. Similar trends can be seen in the bulk modulus of Fe-Ni alloys obtained from *ab initio* calculations [132, 133]. We note that the composition of our Fe-30Ni alloy is very close to that of Invar Fe-35Ni (Fe-26Ni in first-principles calculation [132]), which is elastically the softest among Fe-Ni alloys. Therefore the reason for the lower modulus of our Fe-Ni alloy may be similar to that proposed for Invar alloys, namely their energetically quasidegenerate small-volume/low-moment (LM) and large-volume/high-moment (HM) ground states [42].

2.3.2 Incipient Plasticity

Clear pop-in events can be observed in all four alloys, as shown in the representative nanoindentation load-displacement curves in Fig. 2.2. The pop-in statistics (cumulative probability versus pop-in load P_{pop-in}) for the four alloys are displayed in Fig. 2.3, where each curve contains data from more than 100 nanoindentation tests performed at different locations on the specimen surface. The four curves exhibit the same trends with smooth ‘S’ shapes in which the probability of pop-in increases after a critical load and then reaches 100% relatively quickly. When the cumulative probability approaches unity, it is often the case that the theoretical strength for dislocation

nucleation is approached, so an anisotropic elastic contact analysis is needed to convert the saturation pop-in loads to resolved shear stresses under the indenter. However, the slopes for two of the curves, Fe30Ni and Fe15Cr, are not as steep as the others. One possible reason for this might be that the pop-in is a result of the sudden motion of pre-existing dislocations in the highly stressed zone rather than the nucleation of new dislocations [10, 56]. The critical stress for defect-assisted events is expected to be about an order of magnitude lower than τ_{th}, thus those curves in which there is an influence of heterogeneous nucleation are expected to have long tails at low pop-in loads. When pop-ins occur at large loads, the highly stressed volume under the indenter is also large, thereby increasing the probability of encountering pre-existing defects [31]. This may be the case in Fe-15Cr given that its pop-in load is the highest of the four alloys. In contrast, the pop-in loads of Fe-30Ni are considerably lower, so its curve may be representative of a higher pre-existing defect density. A detailed discussion and mathematical modeling of these two pop-in mechanisms will be given in Section 2.4.3.

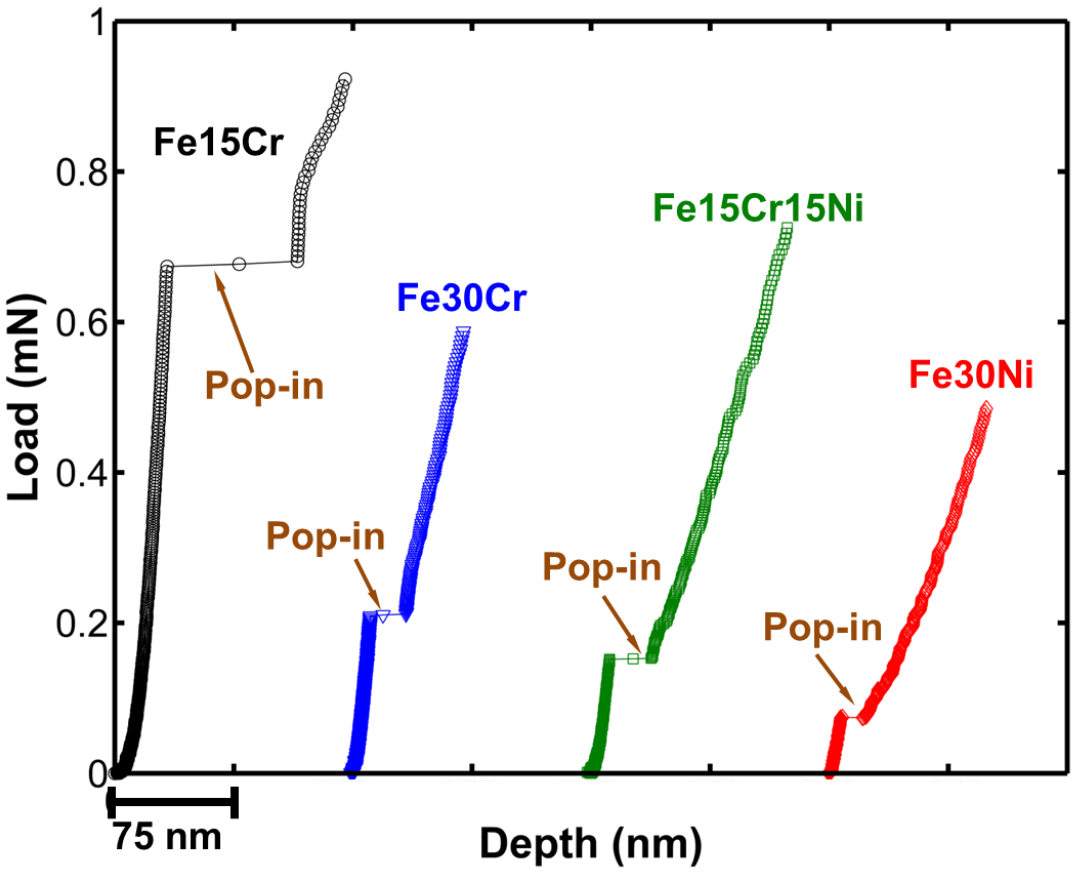

Fig. 2.2 Representative nanoindentation load-displacement curves for Fe-15Cr, Fe-30Cr, Fe-15Cr-15Ni and Fe-30Ni alloys. The curves are shifted laterally for clear visualization. The indenter radius is 400 nm.

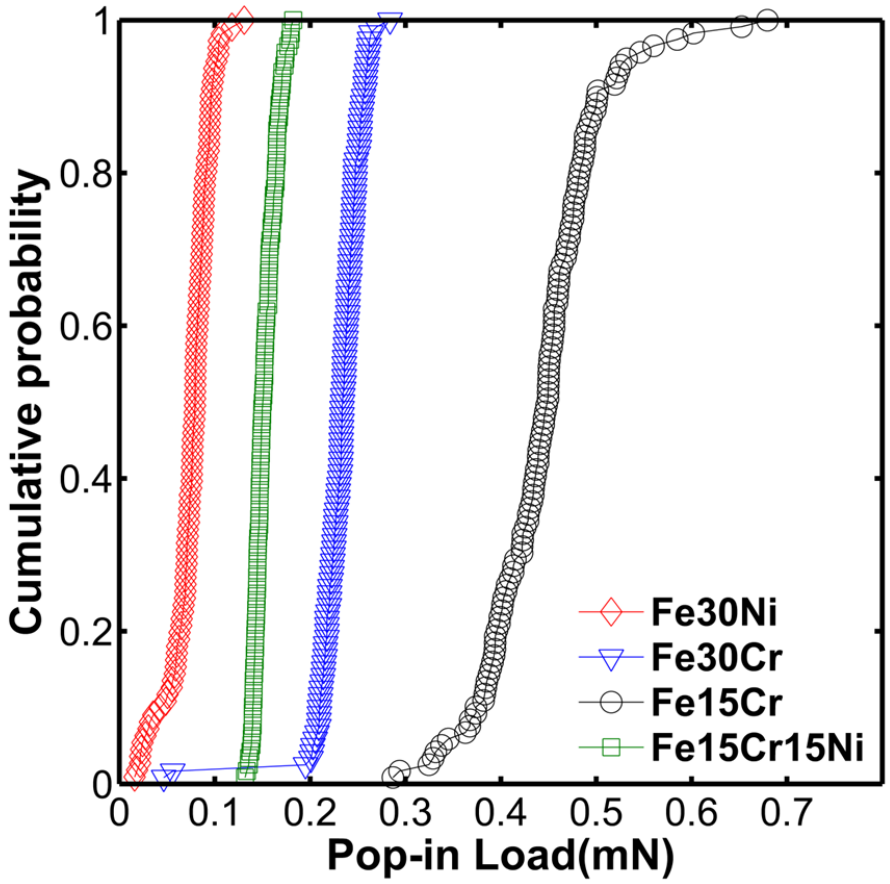

Fig 2.3 Dependence of the cumulative pop-in probability on pop-in load for the four investigated alloys under spherical nanoindentation.

2.3.3 Slip trace analysis

Surface slip trace analysis is the primary method to determine the slip systems that are active inside a crystal. In uniaxial tests, it is found that the slip direction is always <111> in BCC crystals while the slip plane can be the most densely packed plane {110} or the main stacking fault plane {112}. Although {123} slip plane is a possible candidate in some BCC metals, it has not been observed in Fe-Cr or Fe-Cr-Ni alloy [134]. In FCC crystals the slip system is {111}<110> (full dislocation) or {111}<112> (partial dislocation). We now investigate the slip traces created by spherical indentation.

Indentation tests were conducted on (001) and $(\bar{1}10)$ surfaces and the slip traces were imaged in an optical microscope as shown in Fig. 2.4. Within a given crystal structure, BCC or FCC, the slip trace patterns were identical regardless of alloy composition (e.g., Fe-15Cr and Fe-30Cr exhibited the same patterns). Therefore, we provide only one (representative) figure for each orientation and crystal structure. As shown in Fig. 2.4a, (001) BCC specimens produce rectangular slip trace pattern with edges inclined at ±45˚ to [001] axis. The slip trace pattern on $(\bar{1}10)$ BCC specimens is presented in Fig. 2.4b. The pattern is diamond shaped with an angle α between the two nonparallel edges of about 43˚. The pattern on (001) FCC specimens is rectangular and similar to that on (001) BCC as shown in Fig. 2.4c. However, the patterns on $(\bar{1}10)$ FCC are more complicated (Fig. 2.4d), and exhibit two different sets of slip traces that might be caused by two different slip systems. One set is parallel to the $[110]$ axis while the other is "X"-shaped with an angle α of about 73˚.

A slip trace on an indentation surface is the intersection of a slip plane and the indentation surface. As a result, from a geometrical analysis, it is possible to predict the shape and symmetry of the slip traces for certain assumed slip systems. We calculated the slip traces for all possible slip systems in BCC and FCC specimens and the predicted patterns are presented in Fig. 2.5 with the corresponding slip systems. Upon comparison with the experimental traces, it is concluded that the activated slip systems are $(112)[11\bar{1}]$, $(11\bar{2})[\overline{111}]$, $(1\bar{1}2)[1\overline{11}]$ and $(\bar{1}12)[\bar{1}1\bar{1}]$ for (001) BCC ($\alpha = 90°$) and $(121)[1\bar{1}1]$, $(12\bar{1})[\bar{1}11]$, $(211)[\bar{1}11]$, $(21\bar{1})[1\bar{1}1]$ ($\alpha = 50°$) for $(\bar{1}10)$ BCC. Therefore, the slip system in Fe-15Cr and Fe-30Cr is $< 112 > [111]$ for both orientations. Similarly, for the FCC alloys, the activated slip planes are found to be (111), $(1\bar{1}1)$, $(11\bar{1})$ and $(\bar{1}11)$ during (001) and $(\bar{1}10)$ indentation, but the slip directions cannot be unambiguously determined. In previous research on other Fe-Ni alloys (Fe-31Ni and Fe-33Ni), {111}<110> dislocations were observed via high-resolution transmission electron

microscopy[135]; therefore, in what follows we assume the {111}<110> slip system for further analysis.

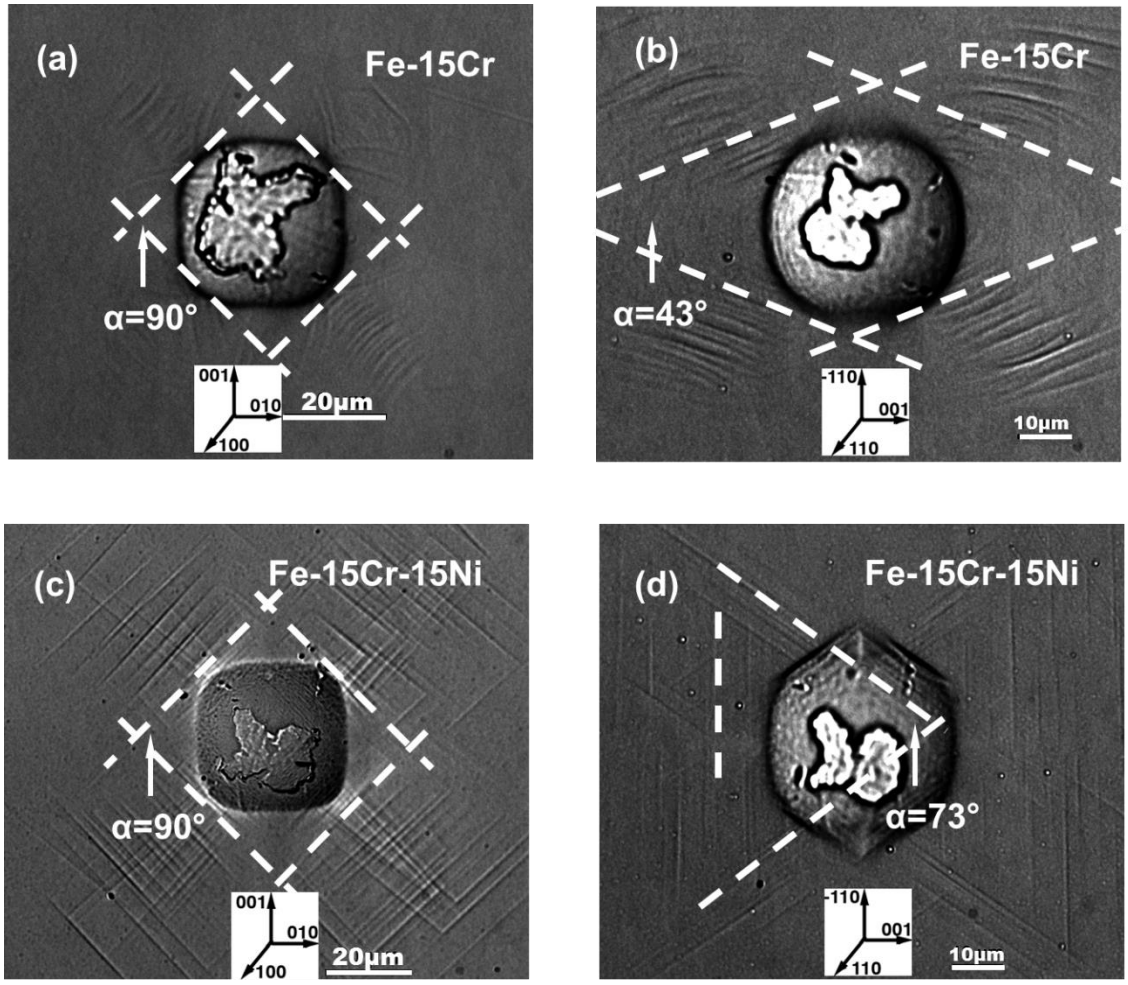

Fig. 2.4 Slip trace patterns from microindentation for (a) (001) Fe-15Cr, (b) $(1\bar{1}0)$ Fe-15Cr, (c) (001) Fe-15Cr-15Ni, and (d) $(1\bar{1}0)$ Fe-15Cr-15Ni. The white dashed lines represent the slip trace patterns. α is the angle between two sets of non-parallel slip traces.

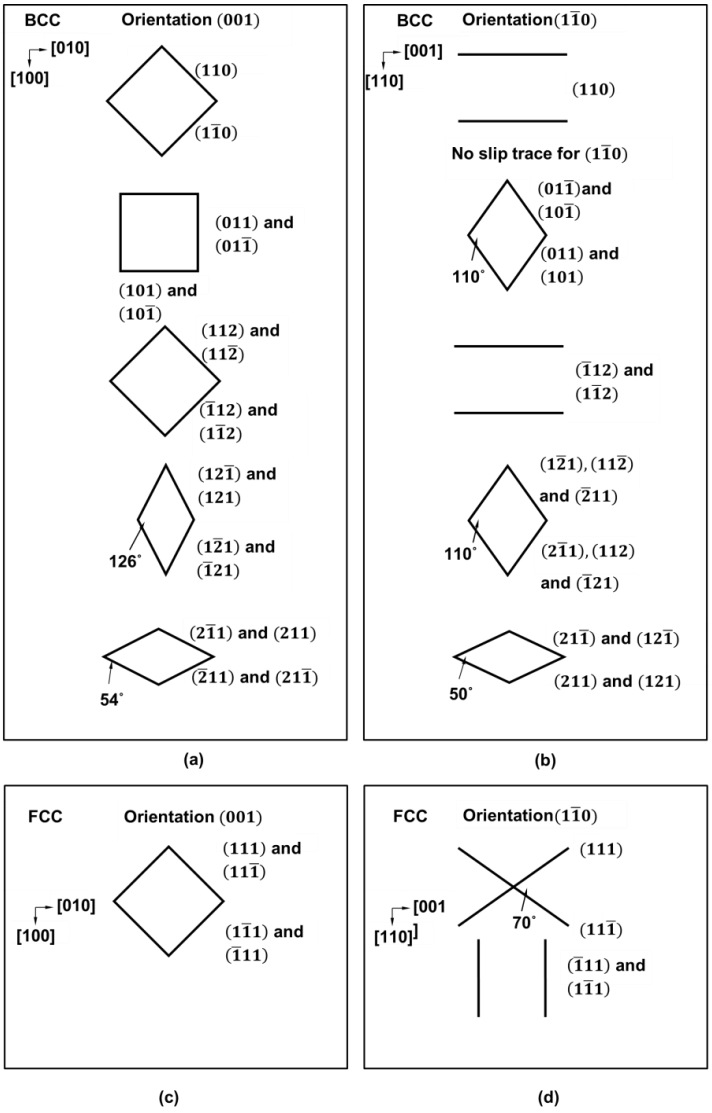

Fig 2.5 All possible slip traces for indentation on (001) and $(\bar{1}10)$ for FCC and BCC specimens from theoretical prediction based on geometric construction. The corresponding slip planes are denoted besides each slip trace. Based on a comparison with experimental slip traces, it is concluded that the activated slip systems are $(112)[11\bar{1}]$, $(11\bar{2})[\bar{1}\bar{1}\bar{1}]$, $(1\bar{1}2)[1\bar{1}\bar{1}]$ and $(\bar{1}12)[1\bar{1}1]$ for (001) BCC and $(121)[1\bar{1}1]$, $(12\bar{1})[\bar{1}11]$, $(211)[\bar{1}11]$, $(21\bar{1})[1\bar{1}1]$ for $(\bar{1}10)$ BCC. The activated slip planes are $\{111\}$ for both FCC alloys.

It is noted that in our FCC alloys the slip traces are straight and coarse while those in the BCC alloys are wavy and fine. This difference agrees with patterns observed in previous tension and compression tests [136, 137]. Wavy slip has been ascribed to non-planar cross-slip of screw dislocations in BCC metals [e.g., 45]. Since there are various possible slip planes including {110}, {112} and other high index planes, the screw dislocation after nucleation may move by a recombination-dissociation glide mechanism which breaks into small segments of collinear glide on a {110}-{112} neighboring plane pair so that the macroscopic average slip traces, comprised of elementary steps from several different planes, are wavy and fine. As shown in Fig. 2.4b, the average experimental α is 43° for $(1\bar{1}0)$ nanoindentation on BCC Fe-15Cr. This corresponds to the predicted angle α of 50 °for slip on {112} plane (Fig. 2.5b). In contrast, FCC crystal has only one slip plane ({111} single glide) and the Peierls-Nabarro resistance is small which leads to less cross-slip and straight and coarse slip traces.

The above analysis is based purely on the geometric features of slip, which allows us to infer the slip systems that are likely activated during indentation. However, from a mechanical viewpoint, we envision a transition from dislocation-nucleation-controlled to continuum-slip deformation modes as the indentation depth increases. Therefore, to obtain a more detailed understanding of the relationship between slip traces and deformation mechanisms, next we conduct anisotropic Hertzian contact analysis and slip-based crystal plasticity modeling for our four alloys.

2.4. Discussion

2.4.1 Anisotropic elastic contact analysis

If no strength-reducing defects are present in the volume sampled, the pop-ins observed in Fig. 2.2 result from homogeneous nucleation of dislocations when the maximum resolved shear stress reaches the theoretical strength τ_{th}. Upon further loading,

these dislocations will multiply and form continuous slip fields that eventually lead to the observed slip traces on the indented surfaces. Therefore in this section, we first calculate the maximum resolved shear stress and its location underneath the indenter for all possible slip systems during elastic contact. This requires an anisotropic indentation analysis to calculate the indentation Schmid factor (ISF). The ISF is defined as the ratio of maximum resolved shear stress among all possible slip systems τ_{rss}^{max} to the maximum contact pressure p_0 under the Hertzian contact[18]:

$$S = \frac{\tau_{rss}^{max}}{p_0}, \tag{2-5}$$

where $\tau_{rss}^{max} = \max_{(\alpha)}\{\sigma_{ij} s_i^{(\alpha)} m_j^{(\alpha)}\}$ and s_i and m_j are the slip direction and the normal to the slip plane. The repeated subscripts imply the usual summation convention. p_0 is given by Hertzian contact mechanics as:

$$p_0 = \left(\frac{6PE^{*2}}{\pi^3 R^2}\right)^{1/3} \tag{2-6}$$

where P is the applied load and R is the indenter radius.

The Stroh formalism and two-dimensional Fourier transform are applied in order to derive the analytical stress field in elastic anisotropic solid under Hertzian contact. With the entire stress fields obtained, a search for the maximum ISF in Eq. (2-5) is conducted using the Nelder-Mead simplex algorithm for a given set of slip systems, and the corresponding slip system and its location determined. This method has been successfully applied to predict dislocation nucleation and the first pop-in event in NiAl[18], Mg [117] and α-Ti [118] alloys. Here we use this method, along with the elastic constants obtained from ultrasonic measurements, to calculate the largest and the second largest ISFs for our four alloys in the (001) and $(\bar{1}10)$ orientations, and the results are given in Table 2.3. For the two sets of slip systems in the BCC alloys, the largest ISFs are within 9% of each other and the maximum resolved shear stress on {112} is equal to

or larger than that on {110} for both indentation orientations. Therefore, without knowing the corresponding theoretical strengths, the ISF analysis alone is unable to uniquely determine on which slip system dislocation nucleation will occur first.

Table 2.3 Largest and second largest indentation Schmid factors for the two possible sets of slip systems in the four alloys. Those for the activated slip systems are shown underlined.

Material	Indentation Plane	Slip System	Largest ISF	2nd Largest ISF
Fe-15Cr	[001]	{110}<111>	0.249	0.153
Fe-15Cr	[001]	{112}<111>	<u>0.264</u>	0.215
Fe-15Cr	$[1\bar{1}0]$	{110}<111>	0.275	0.195
Fe-15Cr	$[1\bar{1}0]$	{112}<111>	0.295	<u>0.229</u>
Fe-30Cr	[001]	{110}<111>	0.257	0.224
Fe-30Cr	[001]	{112}<111>	<u>0.275</u>	0.213
Fe-30Cr	$[1\bar{1}0]$	{110}<111>	0.272	0.195
Fe-30Cr	$[1\bar{1}0]$	{112}<111>	0.298	<u>0.212</u>
Fe-15Cr-15Ni	[001]	{111}<110>	<u>0.230</u>	0.183
Fe-15Cr-15Ni	$[1\bar{1}0]$	{111}<110>	<u>0.254</u>	<u>0.184</u>
Fe-30Ni	[001]	{111}<110>	<u>0.233</u>	0.185
Fe-30Ni	$[1\bar{1}0]$	{111}<110>	<u>0.260</u>	<u>0.183</u>

For spherical indentation, the contact response transitions from elastic, to elastic-plastic, to fully plastic behavior as the ratio of contact radius to indenter radius increases. The elastic contact analysis presented here predicts where and on which slip systems the first several dislocations are nucleated. It is reasonable to expect that subsequent dislocation multiplication will occur at or near these sites of maximum resolved shear

stress. This conjecture has been confirmed by a recent TEM study of Ti single crystal [118], which found that, indeed, dislocation loops formed at the locations predicted by the elastic contact ISF analysis. Consequently, ISF analysis will provide important guidance on how slip traces form under indents. Obviously, the stress fields in the fully plastic state are very different from the elastic ones that are considered here. This issue will be addressed in the crystal plasticity simulations in the next section.

We correlated the ISFs and the positions where the resolved shear stress is maximum for the activated slip systems determined in slip trace analysis, as shown in Fig. 2.6. In the BCC alloys, for the different slip systems considered (Table 2.3), it is found that during (001) indentation the activated slip system determined by the slip trace analysis does indeed have the largest ISF, namely, 0.264 for Fe-15Cr and 0.275 for Fe-30Cr. The situation is similar for (001) indentation in the FCC alloys: both ISFs for Fe-15Cr-15Ni and Fe-30Ni are about 0.230. Since there are two kinds of slip trace patterns on the $(\bar{1}10)$ surface, ISFs for both of the corresponding activated slip systems were calculated, which are the largest and second largest in the set of slip systems considered. The trace parallel to the [110] axis has the largest ISF while the ISF of the "X"-shaped trace has the second largest ISF among the {111}<110> slip systems. Such analysis indicates that dislocations nucleate, and subsequently multiply during slip deformation, at or near the sites where the shear stresses are maximum. However, we also note that ISFs are 0.229 or 0.212, the second largest ISF in {112}<111> slip system for $(\bar{1}10)$ BCC. Also the second largest ISF in {112}<111> slip system is smaller than the largest one in {110}<111> slip system (about 0.275).

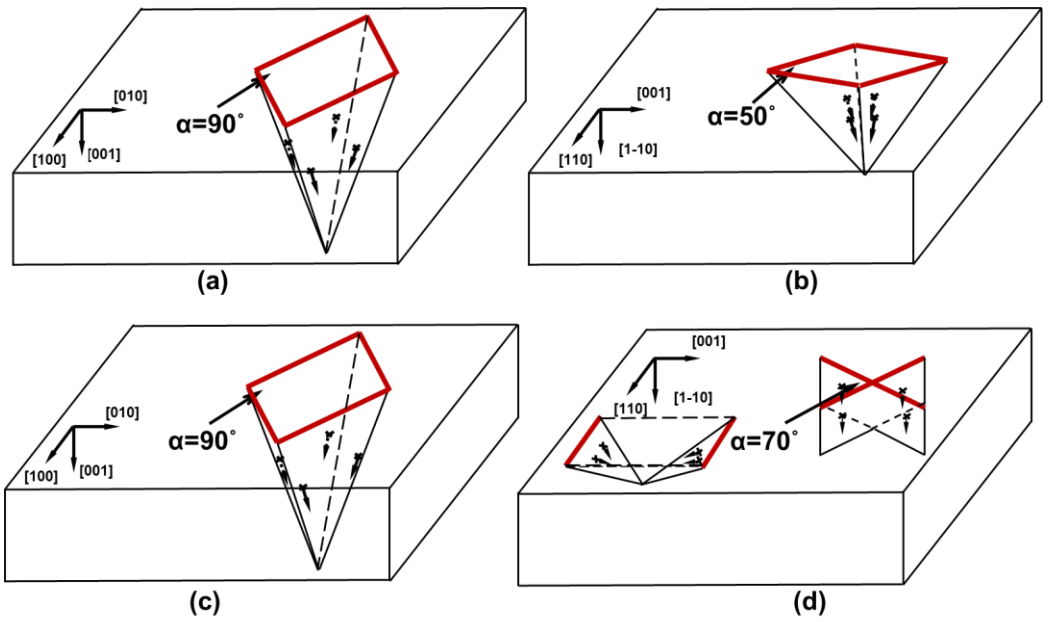

Fig. 2.6 Schematic diagrams showing locations of the maximum resolved shear stress, slip plane, slip direction and slip trace patterns from ISF analysis for (a) (001) BCC crystal, (b) $(\bar{1}10)$ BCC crystal, (c) (001) FCC crystal, and (d) $(\bar{1}10)$ FCC crystal. The red lines on the indentation surface are the slip traces. α is the angle between two sets of non-parallel slip traces.

Since ISFs are determined for the activated slip system under (001) indentation, we are able to obtain the theoretical strength τ_{th} using

$$\tau_{th} = S\left(\frac{6P_{cr}E^{*2}}{\pi^3 R^2}\right)^{1/3}. \tag{2-7}$$

We define the critical load P_{cr} as the pop-in load at the cumulative probability of 90%. The critical loads thus obtained from Fig. 2.3 are 0.501mN for Fe-15Cr, 0.235mN for Fe-30Cr, 0.160mN for Fe-15Cr-15Ni, and 0.0958mN for Fe-30Ni. The theoretical strengths calculated using these pop-in loads and Eq. 2-7 are listed in Table 4. In terms of their shear moduli, they are $\sim\mu/15$, where μ is the shear modulus on the corresponding slip system, expressed as $\mu = c_{ijkl}p_i q_j p_k q_l$ where c_{ijkl} is the stiffness tensor [138].

These values are in the typical range of theoretical strengths, $\mu/30 - \mu/5$, which implies homogenous dislocation nucleation.

Table 2.4 Theoretical strength τ_{th} of the four alloys determined from pop-in analysis.

	Fe-15Cr	Fe-30Cr	Fe-15Cr-15Ni	Fe-30Ni
τ_{th} (GPa)	7.21	6.39	4.17	2.98

2.4.2 Crystal plasticity simulations for the slip trace analysis

Although slip trace analysis combined with anisotropic contact analysis is a reasonably accurate way to determine the activated slip systems, as shown in the preceding section, it fails to provide important details, e.g., macroscopic strain in the plastic zone. In order to better understand the plastic deformation of the four types of alloys and verify the conclusion from the slip trace analysis, a slip-based crystal plasticity model was employed to investigate the slip strain field in the fully plastic state.

Our finite-element analysis (FEA) was conducted with commercial software ABAQUS with a user-material subroutine UMAT incorporating single crystal plasticity [139]. The total deformation gradient **F** can be expressed as a multiplicative decomposition:

$$\mathbf{F} = \mathbf{F}^e\mathbf{F}^p \tag{2-8}$$

in which $\mathbf{F}^p$ is the plastic part solely due to crystalline slip on a given set of slip systems and $\mathbf{F}^e$ represents lattice stretching, rotation and rigid body motion. The rate of change of $\mathbf{F}^p$ is related to the sum of the slip rate $\dot{\gamma}^{(\alpha)}$ by

$$\dot{\mathbf{F}}^p\mathbf{F}^{p^{-1}} = \sum_\alpha \dot{\gamma}^{(\alpha)}\mathbf{s}^{(\alpha)} \otimes \mathbf{m}^{(\alpha)} \tag{2-9}$$

in which $\dot{\gamma}^{(\alpha)}$, $\mathbf{s}^{(\alpha)}$ and $\mathbf{m}^{(\alpha)}$ are the slip rate, the slip direction and the slip plane normal of the αth slip system, respectively.

The slip rate is a function of the resolved shear stress $\tau^{(\alpha)}$ and the strength of that slip system $\tau_{flow}^{(\alpha)}$. Following the work in [140, 141], the plastic flow equation is taken as a power-law form:

$$\dot{\gamma}^{(\alpha)} = \dot{\gamma}_0 \left| \frac{\tau^{(\alpha)}}{\tau_{flow}^{(\alpha)}} \right|^n \operatorname{sgn}(\tau^{(\alpha)}) \tag{2-10}$$

where $\dot{\gamma}_0$ is the characteristic strain rate, $\tau^{(\alpha)}$ is the resolved shear stress, $\dot{\tau}_{flow}^{(\alpha)}$ is the flow strength of the αth slip system and n is the stress component. Since our main goal here is to describe dislocation slip in anisotropic single crystals during nanoindentation rather than strengthening effects, work hardening during plastic deformation was not taken into consideration in FEM simulation.

The finite element model we used has the geometric symmetry associated with the rigid sphere indenter and the crystallographic symmetry of the indented crystal, which allows us to use just half of the deformable crystal in our simulations. The bottom of the crystal is fixed along *z*-axis. Symmetric boundary condition is applied to the cross-sectional surface about *y*-axis. The contact between the indenter and the crystal is frictionless. The mesh has finer elements near the indenter. The elastic constants used are those in Table 2.2. Regarding the parameters for slip, the initial slip strength τ_0 is determined from the hardness of the alloys from nanoindentation. According to the Tabor relation, the tensile strength can be expressed as $\sigma = H/\alpha$, in which α is usually equal to 3. Then we use the Taylor factor M (approximately 3 for both BCC and FCC crystals) to predict the slip strength τ_0 based on the tensile strength by $\tau = \sigma/M$ [1]. Thus τ_0 is 183MPa for Fe-15Cr, 340MPa for Fe-30Cr, 162MPa for Fe-15Cr-15Ni and 158MPa for

Fe-30Ni. The other slip parameters are n and $\dot{\gamma}_0$ which are 20 and 0.001 s^{-1}, respectively. We simulated two different indentation orientations: (001) and $(\bar{1}10)$.

Fig. 2.7 shows the sum of "normalized" shear strain distributions ($\gamma_{norm} = \sum|\gamma^{(\alpha)}|\,(R/a)$) considering all the activated slip systems obtained from the previous slip trace analysis. The slip systems added together for the BCC alloys include (112) $[11\bar{1}]$, $(11\bar{2})[\overline{111}]$, $(1\bar{1}2)[1\overline{11}]$ and $(\bar{1}12)[\bar{1}1\bar{1}]$ for (001) indentation, and $(121)[1\bar{1}1]$, $(12\bar{1})[\bar{1}11]$, $(211)[\bar{1}11]$ and $(21\bar{1})[1\bar{1}1]$ for $(\bar{1}10)$ indentation. For the FCC alloys, the slip systems added together are $(111)[1\bar{1}0]$, $(1\bar{1}1)[110]$, $(11\bar{1})[101]$ and $(\bar{1}11)[110]$. Here a/R determines the magnitude of the indentation strain field, so it is used to compare the slip strains. Because the slip traces are formed by the intersection of gliding dislocations and the free surface, the slip traces will not follow all the slip strain contour lines; rather they correspond to only the outermost contour line, as shown by the white dashed lines in Fig. 2.7. These predicted slip trace patterns agree well with the experimental observations. For (001) BCC, the contour is a 4-fold rosette with $\alpha = 90°$ as shown in Figs. 2.7a and 2.7c. During $(\bar{1}10)$ BCC indentation, as shown in Figs. 2.7b and 2.6d, the slip traces denoted by white dashed lines form a rectangle with an angle α of about 50˚ (43˚ in experiment). The (001) FCC specimens exhibit a 4-fold rosette (Figs. 2.7e and 2.7g) similar to that in (001) BCC specimens. In the case of $(\bar{1}10)$ FCC, two types of slip trace pattern are obtained (Figs. 2.7f and 2.7h). One has edges parallel to the [110] axis. The other has a dog-bone shape with an angle α of about 65˚ (the experimental value of α is ~73˚). These results show that FEM simulation provides additional insight into the deformation occurring during the slip stage of indentation and that both sets of predicted slip trace patterns (from FEM and ISF analyses) are consistent with the experimentally observed patterns. Consequently, although the stochastic deformation behavior that occurs after the first pop-in and before continuum plasticity sets in cannot be modeled, the same types of slip traces that are predicted from these two

limit cases (i.e., elastic stress analysis in the previous section and the finite element simulations in this section) validate our slip trace analysis.

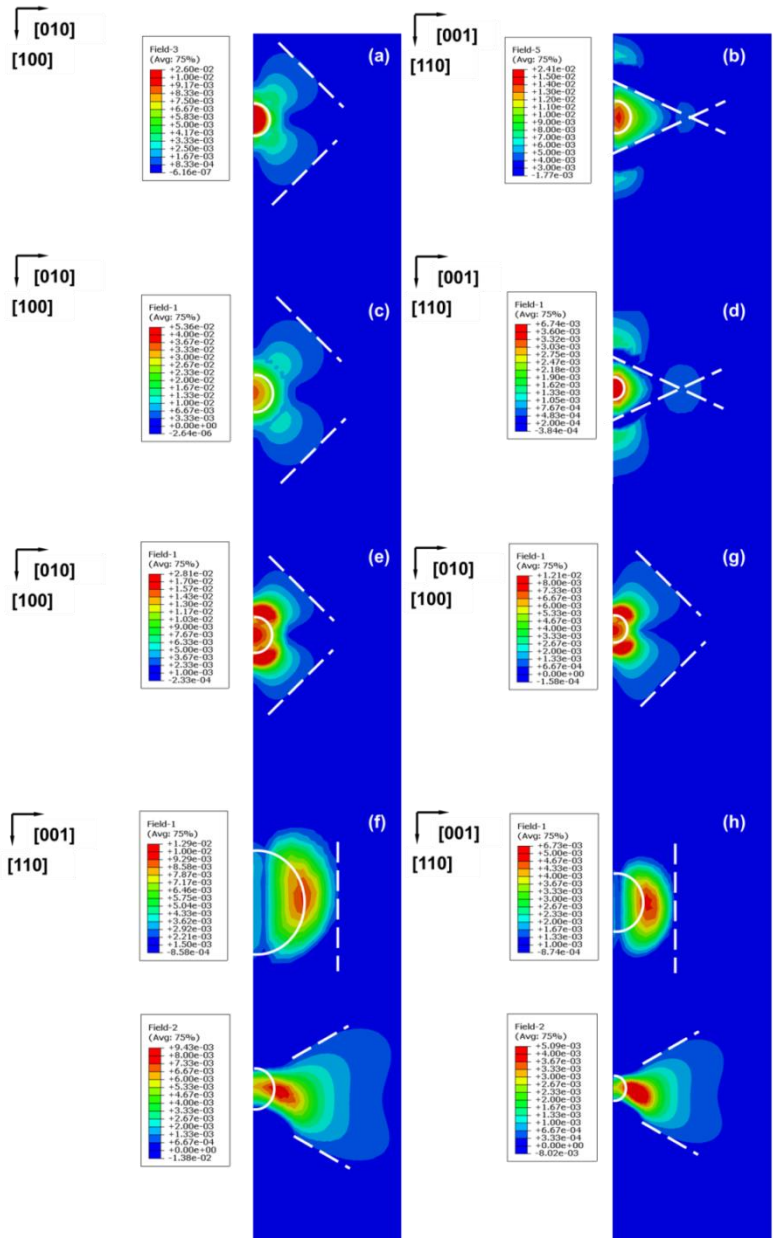

Figure 2.7 Normalized slip shear strain from finite element method for (a) (001) Fe-15Cr, (b) $(\bar{1}10)$ Fe-15Cr, (c) (001) Fe-30Cr, (d) $(\bar{1}10)$ Fe-30Cr, (e) (001) Fe-15Cr-15Ni, (f) $(\bar{1}10)$ Fe-15Cr-15Ni, (g) (001) Fe-30Ni, and (h) $(\bar{1}10)$ Fe-30Ni. Refer to the text for the definition of slip shear strain. The white solid circles present the contact area of the indenter. The white dashed lines are the edges of contour which corresponds to the slip trace.

2.4.3 Homogenous vs. heterogeneous pop-in mechanisms

In a defect-free single crystal, the mechanism for the first pop-in event is homogenous dislocation nucleation, which is governed by thermal statistics in the defect-free and highly stressed zone under the indenter. When the applied resolved shear stress is a little lower than the theoretical strength τ_{th}, the energy barrier for dislocation nucleation can be expressed as $\Delta\Pi = A\left(1 - \tau_{appl}/\tau_{th}\right)^{m}$, based on a number of atomistic and Peierls-Nabbaro dislocation analyses. The fitting parameter A is found to be in the range $5 - 15\mu b^3$ where μ is the shear modulus and b is the magnitude of the Burgers vector, and the exponent m is in the range of 1.5-4.5. Based on the first-order kinetics, the cumulative probability for homogenous dislocation nucleation on all available slip systems can be expressed as follows

$$f_{hom} = 1 - exp\left\langle -\dot{n_0} \sum_{\alpha} \int_0^{P_{pop-in}} \iiint_{\Omega} \exp\left\{ -\frac{\Delta\Pi^{(\alpha)}\left[\tau_{\mathrm{RSS}}^{(\alpha)}\right]}{k_{\mathrm{B}}T} \right\} d\Omega \, \frac{dP}{\dot{P}} \right\rangle \qquad (2\text{-}11)$$

in which $\dot{n_0}$ is an attempt frequency per unit volume, k_B is Boltzmann constant, T is the absolute temperature, and P is the indentation load. This homogenous dislocation nucleation model matches well with the indentation experiments when the stressed volume is small in specimens with low pre-existing defect density.

However, as noted before, some of our cumulative probability curves have less steep slopes and show slight deviations from "S" shape (Fig. 2.3). In these cases, it is expected that the spatial statistics of pre-existing defects in the specimens may control the first pop-in event and onset of plasticity. Following [31], V_d is defined as the volume where the applied resolved shear stress, τ_{appl}, reaches the defect strength, τ_{defect}. The probability of finding no pre-existing defect in V_d is assumed to obey the Poisson distribution and thus the cumulative probability for heterogeneous pop-in mechanism is given by

$$f_{het} = 1 - exp\left[-\rho_{defect} V_d\right] \qquad (2\text{-}12)$$

where ρ_{defect} is the pre-existing defect density in the specimen.

Our previous work developed a combined thermal-spatial statistics model to unify the homogenous and heterogeneous mechanisms, which are treated as independent events [35]. The cumulative pop-in probability can be obtained from Eqs. (2-11) and (2-12):

$$f_{total} = 1 - exp\,\langle -\dot{n_0} \sum_{\alpha} \int_0^{P_{pop-in}} \iiint_{\Omega} \exp\left\{ -\frac{\Delta\Pi^{(\alpha)}\left[\tau_{\mathrm{RSS}}^{(\alpha)}\right]}{k_{\mathrm{B}}T} \right\} d\Omega \; \frac{dP}{\dot{P}} \rangle$$
$$\times\, exp\left[-\rho_{defect} V_d\right] \qquad (2-13)$$

in which the first exponential term accounts for homogenous pop-in mechanism, Eq. (11), and the last exponential term accounts for heterogeneous pop-in, Eq. (2-12). Equation (2-13) has been shown previously to be in excellent agreement with nanoindentation data for Mo and NiAl obtained with spherical indenters having different radii. Here it is applied to obtain estimates of the pre-existing defect density ρ_{defect} in the four alloys. The theoretical strengths used for the fitting are obtained from the calculations in Section 2.4.1. As shown in Fig. 2.8, the predicted curves (Eq. 2-13) match well those from experiments. The fitting results in Table 2.5 show that Fe-30Ni has the highest defect density and Fe-30Cr and Fe-15Cr-15Ni have the lowest defect densities, which are two orders of magnitude lower than that of Fe-30Ni. The defect density of Fe-15Cr is approximately in the middle of these two extremes. These results indicate that, to varying degrees in the four alloys, incipient plasticity involves both thermally activated and the defect-assisted processes. In the case of Fe-30Cr and Fe-15Cr-15Ni, incipient plasticity may be solely due to thermally activated homogenous dislocation nucleation given their low defect densities (0.03 μm^{-3}) while in Fe-30Ni the defect density may be high enough (~3 μm^{-3}) that incipient plasticity occurs by the activation of pre-existing dislocations. Similar statistical distributions are seen also in the yield strengths obtained from small-scale uniaxial tests. For example, Mo-alloy fibers with length l show the largest amount of scatter in yield strengths at intermediate values of $(\rho_{defect})^{0.5} l$, from 0.05 to 0.3 [142].

Clearly, a determination of the pre-existing defect density is important in understanding small-scale mechanical behavior. Usually, this is accomplished experimentally using TEM or X-ray diffraction [143] both of which can be cumbersome. The approach discussed above, where homogenous versus heterogeneous pop-ins are analyzed, provides a simpler way to indirectly infer the pre-existing defect densities.

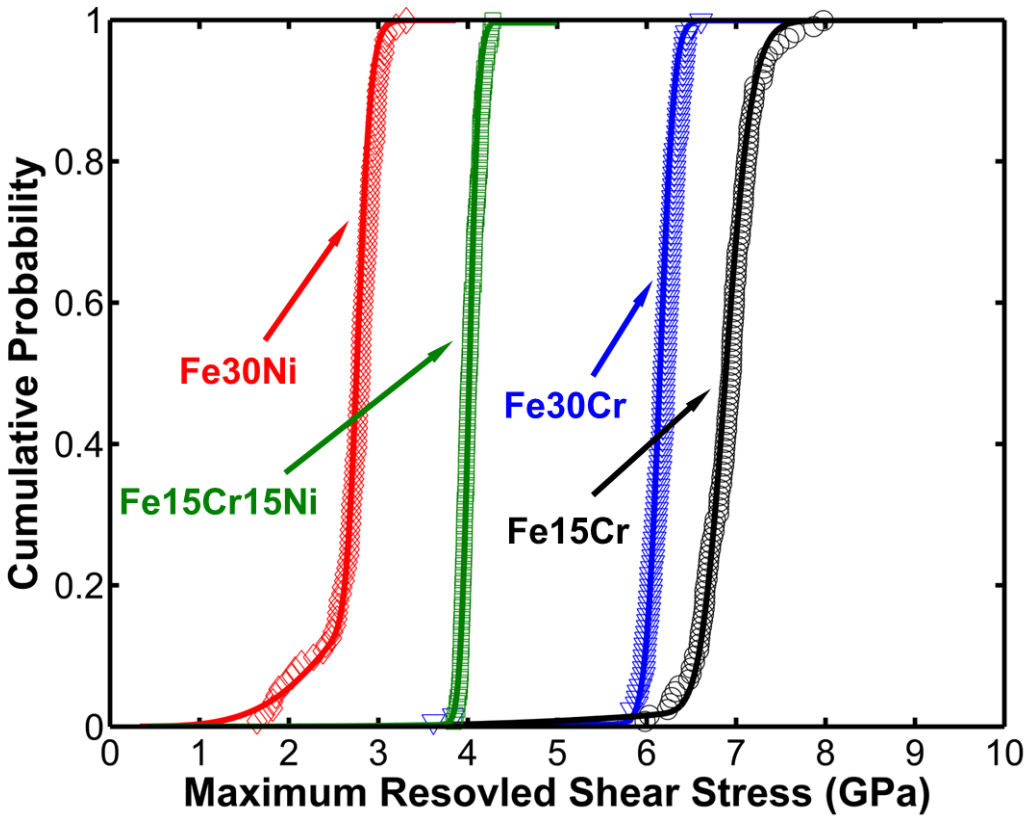

Figure 2.8 Cumulative pop-in probabilities as a function of maximum resolved shear stress for indenter radius of 400nm. The solid lines are predicted pop-in behaviors considering both homogenous and heterogeneous pop-in mechanisms with fitting parameters given in Table 2.5.

Table 2.5 Fitting parameters used in Fig. 8 for the four alloys under spherical indentation with indenter radius of 400 nm. In the fitting, $\tau_{defect} = 0.04\tau_{th}$, and other parameters are obtained from the nanoindentation experiments.

	Fe-15Cr	Fe-30Cr	Fe-15Cr-15Ni	Fe-30Ni
m	4	2.8	2.9	4.2
ρ_{defect} (μm^{-3})	0.1	0.03	0.03	3.1

2.5 Summary and Conclusions

The mechanical properties of model BCC and FCC alloys based on Fe-Cr, Fe-Ni, and Fe-Cr-Ni were experimentally characterized using ultrasonic, nanoindentation, and microindentation techniques. Based on a synergistic analysis of these experiments with simulations and theoretical predictions, the following conclusions were made:

1. The nanoindentation hardness/modulus, measured by continuous stiffness method, are 1.65/181 GPa for Fe-15Cr (BCC), 3.06/193 GPa for Fe-30Cr (BCC), 1.46/156 GPa for Fe-15Cr-15Ni (FCC), and 1.43/136 GPa for Fe-30Ni (FCC). The indentation modulus is consistent with values calculated from the single crystal elastic constants of all four alloys.
2. Slip trace analysis indicates that, during (001) and $(\bar{1}10)$ indentation, slip occurs on the {112} planes in Fe-15Cr and Fe-30Cr (BCC alloys) and on the {111} planes in Fe-15Cr-15Ni and Fe-30Ni (FCC alloys). The activated slip systems determined by slip trace analysis have the largest or second largest ISFs among the set of possible slip systems which confirms that both incipient plasticity (dislocation nucleation) and continuum slip plasticity occur on those slip systems with large ISF or maximum resolved shear stress.
3. More than a hundred nanoindentation tests were performed on (001) surfaces of Fe-15Cr, Fe-30Cr, Fe-15Cr-15Ni and Fe-30Ni single crystals and the distributions of pop-in load measured. From these distributions and anisotropic elastic contact

analysis the theoretical strength τ_{th} was determined to be 7.21GPa for Fe-15Cr, 6.39GPa for Fe-30Cr, 4.17GPa for Fe-15Cr15Ni and 2.98GPa for Fe-30Ni.

4. The pop-in loads were analyzed in terms of homogenous versus heterogeneous mechanisms of incipient plasticity. It was found that the pre-existing defect densities are higher in Fe-30Ni and Fe-15Cr. Therefore, heterogeneous pop-in mechanisms should be taken into account in future microstructure-property analysis of these alloys.

Chapter 3 The investigation of the pop-in mode and the size effect of pop-in excursion

3.1 Introduction

Nanoindentation is a ubiquitous tool to investigate the onset of plasticity at nano-/micrometer[19]. The elastic-plastic transition is always associated with distinct displacement burst/bursts which is called pop-in event on the otherwise continuous load-depth curves (*P-h* curve)[14, 18, 22, 33, 35]. In past research, the 1st pop-in event and related issues were intensively studied, i.e. pop-in mechanism, key factors to pop-in. However it is noted that there are two different pop-in modes: In most of cases there is a single large displacement burst after which the deformation obeys the plastic behavior at continuum level. In contrast, it is also observed that there are multiple successive pop-ins after the 1st pop-in with much smaller excursions. The mechanisms for the two modes are still unclear. In this section, we aim to compare pop-in modes for typical materials with different crystal structures with different indenter radius and thus to have a better understanding of the pop-in mode.

3.2 Result and discussion

First, the pop-in modes of Mo (bcc) and Ni (fcc) are compared at different tip radius as presented in Fig. 3.1[21, 22]. The *P-h* curve of Mo(100) exhibits a very clear pop-in event whose excursion is about 50 nm. Before the 1st pop-in event, the *P-h* curve completely obeys the Hertzian contact theory

$$F_e = \frac{4}{3} E_r (Rh^3)^{0.5} \tag{3-1}$$

which implies the deformation is pure elastic. After the 1st pop-in, the dislocation density increases in order to accommodate the applied strain fields which scale as a/R. Therefore, for spherical indentation on soft materials, eventually a fully plastic deformation stage can be reached, and the corresponding the applied load can be described by the hardness:

$$F_p = AH \tag{3-2}$$

in which A is the contact area and H is the hardness of material. As shown in Fig. 3.2, the contact area $A = \pi a^2 = \pi(R^2 - (R-h)^2) = \pi(2Rh - h^2)$ in which a is the contact radius. Neglecting the higher order term $o(h^2)$, the plastic load can be expressed as follows:

$$F_p = 2\pi HRh \tag{3-3}$$

which implies that there is a linear relationship between the load F and the depth h in plastic deformation.

Fig. 3.1 Typical P-h curves during nanoindentation for (a) Mo(100) with $R = 220$ nm [21] (b) Ni(100) with $R = 220$ nm [21] (c) Ni(100) with $R = 580$ nm [22].

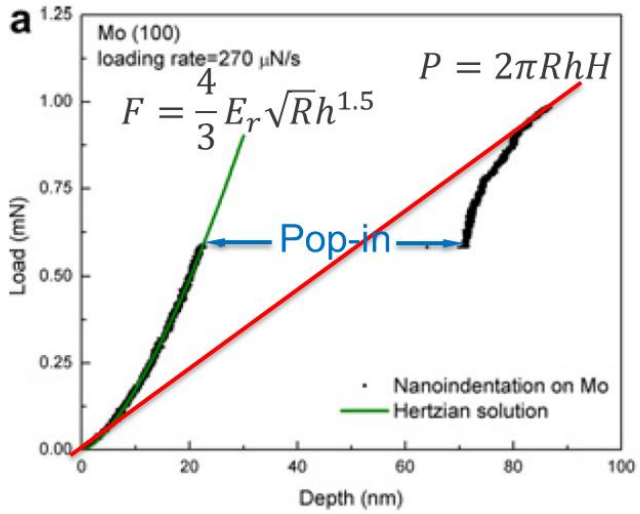
a
Mo (100)
loading rate=270 μN/s
$F = \frac{4}{3} E_r \sqrt{R} h^{1.5}$
$P = 2\pi RhH$
Pop-in
Nanoindentation on Mo
Hertzian solution
Load (mN)
Depth (nm)
0.00
0.25
0.50
0.75
1.00
1.25
0
20
40
60
80
100

(a)

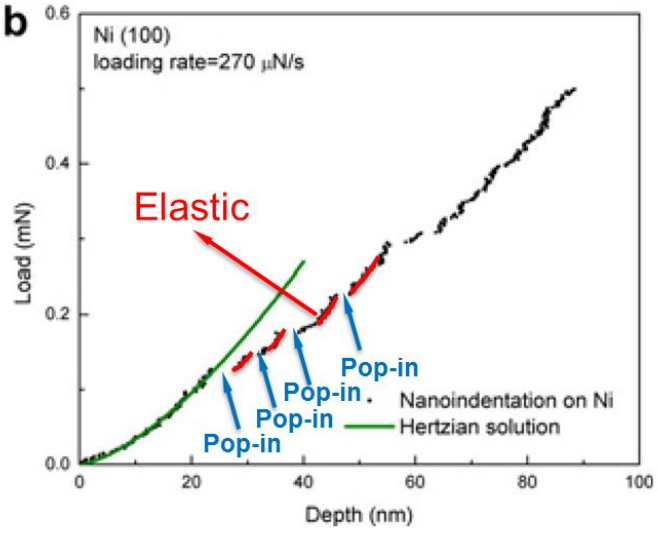
b
Ni (100)
loading rate=270 μN/s
Elastic
Pop-in
Pop-in
Pop-in
Pop-in
Nanoindentation on Ni
Hertzian solution
Load (mN)
Depth (nm)
0.0
0.2
0.4
0.6
0
20
40
60
80
100

(b)

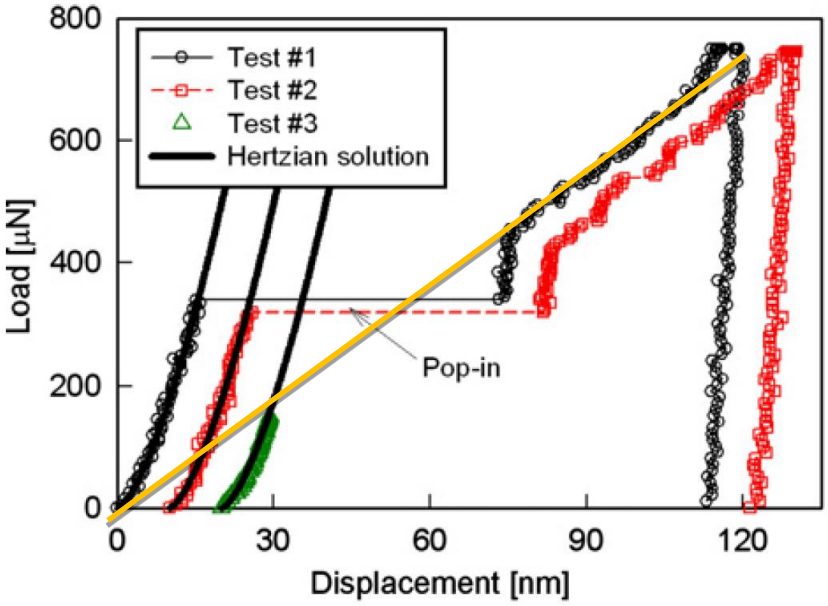
800
600
400
200
0
Load [μN]
0
30
60
90
120
Displacement [nm]
Test #1
Test #2
Test #3
Hertzian solution
Pop-in

(c)

The mode of multiple successive pop-ins can be observed during Ni(100) nanoindentation with tip radius equals to 220 nm as shown in Fig. 3.1b. The excursion Δh is only about 5 nm. After 1st pop-in, the *P-h* curve still can be well fitted by Eq. (3-1) if h is replaced with $h - \Delta h$. The fitting result implies that the deformation is quite possible to be elastic in the high stressed zone. Experiments like unloading test are needed to further prove the conclusion. An explanation based on the dislocation nucleation and movement will be given later. Compared with Fig. 3.1a and b, it can reach a conclusion that the microstructure plays an important role in pop-in mode.

Also another interesting experiment conducted by Shim et al using 580 nm indenter to perform nanoindentation on anneal (100) Ni as presented in Fig. 3.1c. Actually the sample used in Fig. 3.1b and Fig. 3.1c were cut from the same single crystal rod, therefore the initial condition, i.e. preexisted defect density should be exactly same. However, the modes of pop-in are totally different. The result with larger indenter size exhibits one single 65 nm pop-in excursion. Therefore, it seems that the pop-in mode is related to indenter radius, as well as the initial defect density.

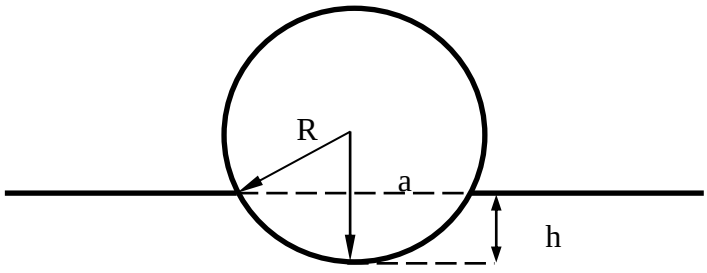

Fig. 3.2 Schematic illustration of the geometry for spherical indenter nanoindentation.

The reason for the size and microstructure effect on the pop-in mode can be explained by the knowledge of the dislocation nucleation and movement. Since the 1st

pop-in stress for the three nanoindentation experiments is in the range of $\frac{G}{30} - \frac{G}{5}$ with G being the shear modulus close with the theoretical strength, it means the onset of the plasticity is due to homogenous dislocation nucleation. When the indenter size R is smaller, the contact radius a is also smaller and thus the size of the stressed zone is smaller. Assuming the dislocation mobility is same in the high stressed zone, the dislocation nucleated beneath the smaller indenter will have higher possibility to escape the high stressed zone where enough stress may be provided for dislocation interaction and multiplication in a moment [42, 144]. The stressed zone became defect-clean again and the further deformation will be elastic obeying Hertzian contact theory, but the effective radius will be larger because of the apparent impression of the specimen surface. However, at that point, the stress in the high stressed zone is very high, near the theoretical stress, and hence the next pop-in event will appear very soon. As a result, the model of several successive pop-in is likely to be appeared at smaller indenter. In contrast, the internal friction for dislocation movement in bcc structure is much higher than that in fcc [54]. For the same indenter size (the same volume of stressed zone), it is more likely to see the dislocation pushed from the high stressed zone to faraway in very short time in fcc metal, i.e. Ni in our research, and thus several successive displacement bursts in P-h curves. In conclusion, the mode of multiple successive pop-ins could not been observed as often as the mode of one large displacement burst, because it requires the nanoindentation experiment to satisfy with two conditions: (1) small indentation size to make the high stressed zone small, and (2) weak internal friction, i.e. in fcc material, and negligible drag or resistance from existing defects.

Further, it is noted that the length of pop-in excursion goes up with the increasing indenter tip radius for the mode of a single large displacement burst. The size effect can be explained by an analytical model with dislocation nucleation mechanism. Assuming that the load at the start of the pop-in is the same as that of the end, Eq. (3-1) and Eq. (3-2) establish the lower and upper bound for the load as a function of indenter displacement.

Right at the pop-in, the maximum resolved shear stress τ_{max} that is responsible for 1st dislocation nucleation is related to *F* through:

$$\tau_{max} = 0.31\left(\frac{6FE_r^2}{\pi^3 R^2}\right)^{\frac{1}{3}} \quad . \tag{3-4}$$

The excursion Δh, can be estimated from the two bounds at different radius:

$$\Delta h = \left[\frac{\tau_{popin}^3 \pi^2}{12*(0.31)^3 E_r^2 H} - \frac{\tau_{popin}^2 \pi}{4*0.31^2 E_r^2}\right] R \tag{3-5}$$

in which τ_{popin} is the maximum resolved shear stress at the pop-in. Eq. (3-5) shows a linear relationship between excursion Δh and R. The reduced modulus and the hardness in Eq. (3-5) can be measured from standard indentation test at a much higher load and found to be 274GPa and 2.22GPa respectively.

The value of τ_{popin} depends on the dislocation nucleation mechanism. There are two kinds of dislocation nucleation mechanism: thermally activated process of homogenous dislocation nucleation and pre-existed defect assisted heterogeneous dislocation nucleation. Homogenous mechanism is that the dislocations are nucleated in crystal when the shear stress approaches the theoretical strength. In contrast, the heterogeneous dislocation nucleation mechanism is that the pre-existed defects sever as the heterogeneous dislocation activation sites to assist the process of dislocation nucleation. At the small radius, the highly stressed volume is so small that it is very likely to be defect-free and thus the dislocation nucleation is believed to be homogenous with $\tau_{popin} = \tau_{th}$. Eq. (3-5) with different presumed pop-in stresses is presented in Fig. 3.3.

When the radius is larger, the excursion matches with the prediction at lower pop-in stress which may be due to the shift of the governing mechanism of pop-in event. The activation stress for heterogeneous dislocation nucleation is generally smaller than the one for homogenous nucleation which is close to theoretical strength. When the indenter size increases, the possibility to find a pre-existed heterogeneous dislocation nucleation site in the stressed volume also increases and thus the governing mechanism shifts to the

combination of homogenous and heterogeneous dislocation nucleation. Because of this mechanism shifting from small to large tip size, the average maximum shear stresses decrease and its fluctuation also increases with the indenter radius as shown in Fig. 3.3. Based on the analysis above, the size effect on the pop-in excursion at large tip radius can be reasonably attributed to the change of the governing pop-in mechanism.

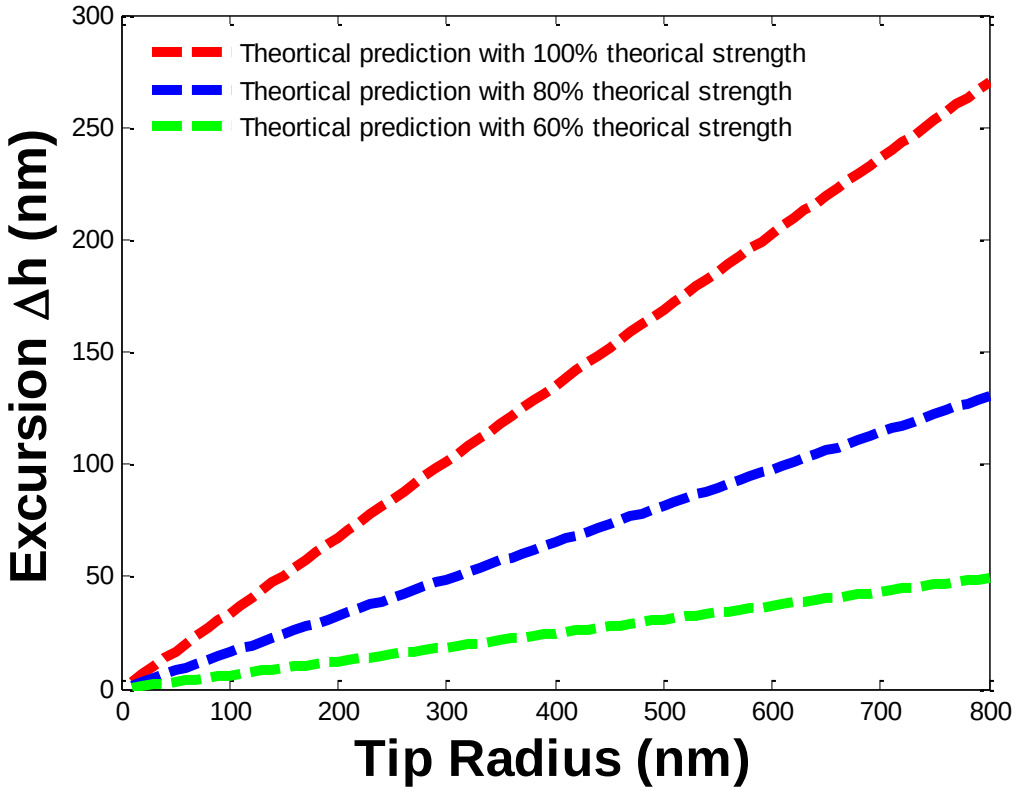

Fig. 3.3 Theoretical prediction of the excursion at different maximum shear stresses in terms of its ratio to the theoretical strength of Mo.

In summary, there are two kinds of pop-in modes: a single large displacement burst and multiple successive pop-ins. The former is more common to see in the past nanoindentation experiments while the later can be observed in fcc sample with a small indenter. The two key factors to have multiple successive pop-ins: small the stressed zone

and high dislocation mobility. Also an analytical model is established to investigate the size effect of pop-in excursion. The effect of the dislocation nucleation mechanism is discussed for the pop-in excursion.

Chapter 4 Failure analysis of pinch-torsion tests as a thermal runaway risk evaluation method of Li-Ion Cells

4.1. Introduction

Lithium-ion batteries are becoming a primary power source in our daily lives through electronic devices (cell phones, tablets and laptops) and transportations (hybrid and electric vehicles, and airplanes). These applications are demanding more power output, higher power density and lower cost, sometimes at the expense of safety. Safety hazard related issues of Li-ion cells have been well documented [145, 146]. Many major field incidents are caused by externally or internally (e.g., manufacturing defects, mechanical abuse, usage abuse, etc.) induced short circuits, which can potentially release the high energy stored in the battery in very short time locally and trigger chemical chain reactions releasing a massive amount of heat. If the battery is not well designed such that the heat cannot be conducted away quickly, thermal runaway could happen and lead to fires and explosions in some extreme cases [147, 148]. Among these safety concerns, internal short circuit (ISCr) under no obvious abuse or external triggers are less understood and very difficult to reproduce experimentally. Therefore, evaluating the thermal runaway risk of Li-ion batteries by experimentally creating ISCr in a controllable and predictable manner has brought broad interests to the field.

In order to evaluate the risk of thermal runaway, many tests have been conducted to simulate ISCr event via internal defect initiation, including forced ISCr test by the Battery Association of Japan, instrumented indentation and nail penetration [149]. We recently reported an improved pinch test method [150-152] that could reproducibly create controllable ISCr in a cell separator where the size of the ISCr spots depends on the loading speed, pinch ball or indenter diameter, and stroke return-voltage. A further development of this pinch test method added a torsional loading component, which exhibited improvement in the effectiveness of creating the ISCr [153]. It was demonstrated in two different commercial Li-ion cells that the torsion facilitated the occurrence of ISCr with lower axial load and smaller ISCr spot size. This method is thus

potentially applicable to very thick batteries, for which the critical loads under pure pinch tests are too large for the standard loading apparatus.

In order to quantitatively relate the pinch-torsion tests to the thermal runaway failure in batteries, it is of critical importance to understand the deformation and failure mechanisms under such loading conditions. For instance, what is the dependence of the critical normal/twist load on the indenter radius, battery thickness, number of electrode/separator layers, and indenter/battery friction condition, among many other factors? Imagine an application of successive pinch and torsion loads, and one can design the loading pattern/history to conveniently identify the failure initiation and optimize the load magnitude to allow a portable evaluation. Motivated by the above considerations, the present paper attempts to develop a computational model for both test methods (pinch-only and pinch-torsion test systems) and make a systematic investigation on the deformation mechanisms to provide insight for the battery safety assessment. In this paper, finite element method (FEM) is used to simulate the strain field and to predict the defect initiation, which was then compared with experiment results. The effect of surface condition was also discussed to optimize the test design. Moreover, the deformation mechanisms were rationalized by an analytical stick-slip model when both contact and torsion were applied.

4.2. Numerical model

The repeating functional unit of a dry Li-ion cell contains an anode layer, a cathode layer, and a separator layer. Since electrolytes used in most Li-ion cells are in liquid phase, they were not included in the finite element models. In addition, the active coatings (graphite and lithium salts) are generally loosely bonded powders on the electrodes, which will be worn into small pieces and pushed away from the highly stressed zone near the indenter tip during the pinch and torsion tests. In fact, our experimental observation revealed that the active coating materials were pushed away

from the contact area after testing (Fig. 4.1). Therefore, the coatings structurally bear little load and will be simply excluded in our FEM setup.

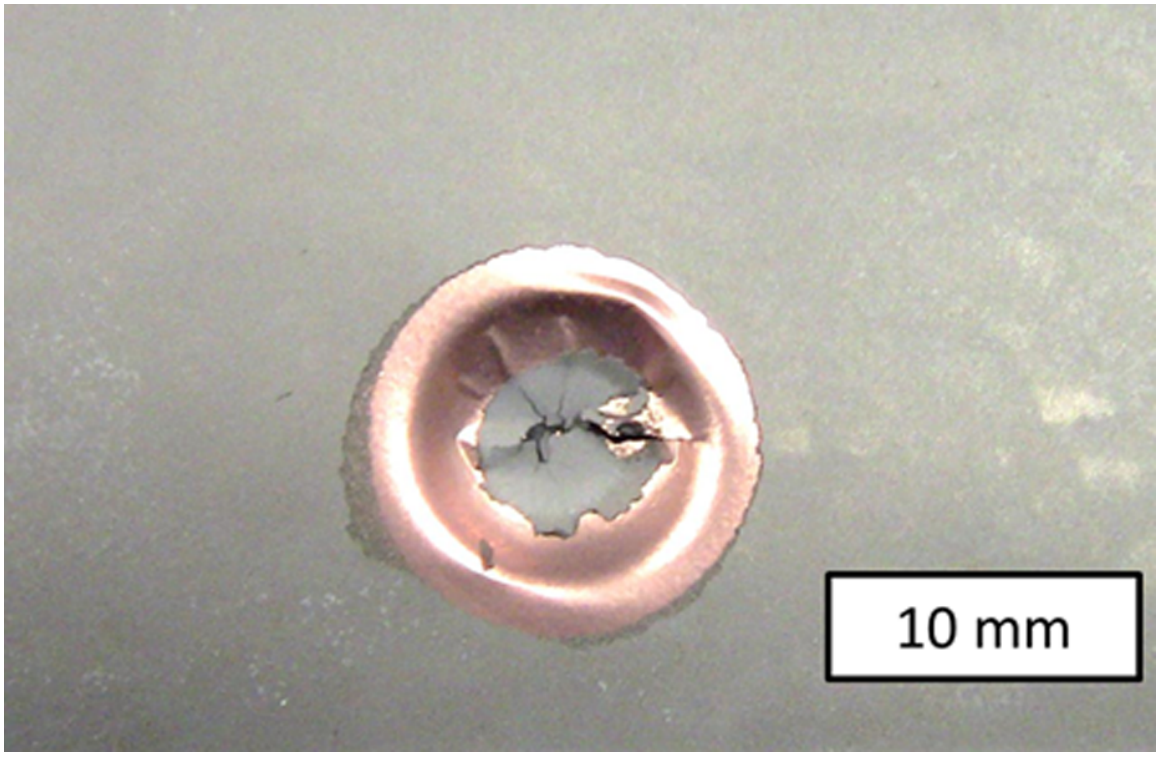

Fig. 4.1 Optical graph of an anode layer after pinch testing showing most of the graphite coating in the indented region was removed during the test (the grey zone is graphite coating).

Fig. 4.2 depicts a three-layer (anode-separator-cathode) unit cell model in the FEM simulation in this study. The material of the top anode layer is Al, the separator layer in the middle is high-density polyethylene (HDPE) and the bottom cathode layer is Cu. The thickness of each layer *h* is 0.02 mm. The two indenters in the pinch and torsion test are modeled as two rigid spheres and the indenter radius is 12.7 mm. The lateral dimension of the unit cell (~ 10 mm) is chosen to be ten times larger than the estimated

contact radius size (~ 1 mm) to eliminate the boundary effects. The bottom indenter is fixed ($u_i = 0, i = 1{\sim}6$) and the top indenter is translated vertically to the unit cell top surface and rotated with displacement boundary condition to represent the twisting in the experiment ($u_2 = 0.9h, u_5 = \theta$ and the rest $u_i = 0$).

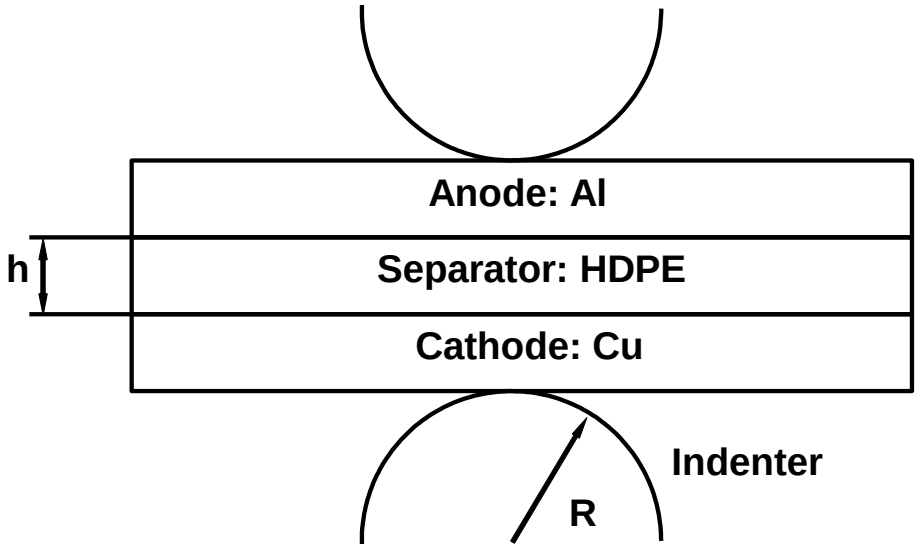

Fig. 4.2 Schematics of the cross section view of a three-layer battery unit cell system under the pinch tests between two spherical indenters.

In nonlinear static finite element analysis (FEA), the strain-displacement equation is $\epsilon_{ij} = \frac{1}{2}(\partial u_i/\partial x_j + \partial u_j/\partial x_i)$ and the stress equilibrium equation is $\partial \sigma_{ij}/\partial x_i + b_j = 0$ in which b_j is the body force. According to the virtual work principle, the equations above can be rewritten as a set of equations $\mathbf{K}(\mathbf{u})\mathbf{u} = \mathbf{F}$ to determine the displacement field and thus strain and stress field after deformation. In the equations, $\mathbf{K}(\mathbf{u})$ is the stiffness matrix and $\mathbf{F}$ is the force vector as a function of the displacement $\mathbf{u}$. The formulas of $\mathbf{K}(\mathbf{u})$ is complex and tedious for our problem with strong nonlinearity. Due to the volume of the paper, we refer our readers to Ref. [154] for more details of the

formulas. It worth noting that $\mathbf{K}(\mathbf{u})$ only relates with mechanical properties of solid, its geometry, the interpolation functions and the nodal positions. As a result, the whole analysis we conducted is pure mechanical, no electronchemistry involved. Our FEA are resolved with commercial finite element package ABAQUS (3DS SIMULIA). Both Al and Cu materials are modeled as elastic-plastic solids with isotropic hardening laws. Materials parameters used in the finite element model are listed in Table 4.1.

Table 4.1. Material properties of Al and Cu foils measured from uniaxial tension tests.

	Aluminum foil	Copper foil
Yield stress, σ_Y(MPa)	180	210
Ultimate stress, σ_u(MPa)	195	230
Yield strain, ϵ_Y	0.017	0.022
Elongation (%)	2.7	3.5

The HDPE material is modeled by the hyperelastic Neo-Hookean material model, where the "strain energy potential" U is based on strain invariants. The form of the Neo-Hookean strain energy potential is

$$U = C_{10}(\bar{I}_1 - 3) + \frac{1}{D_1}(J^{el} - 1)^2 \tag{4-1}$$

where $\bar{I}_1$ is the first deviatoric strain invariant and J^{el} is the elastic volume ration, C_{10} and D_1 are the model parameters determined from the HDPE material stress-strain curve measured from uniaxial tensile test. HDPE materials show various behavior in uniaxial tensile test e.g monotonic hardening [155] and softening effect where the stress decreases with increasing strain after yield due to the reorientation phenomenon [156]. Representative stress-strain curves of HDPE are shown in Fig. 4.3. In our analysis, discrete data points from uniaxial tension test are input in the material definition section in ABAQUS.

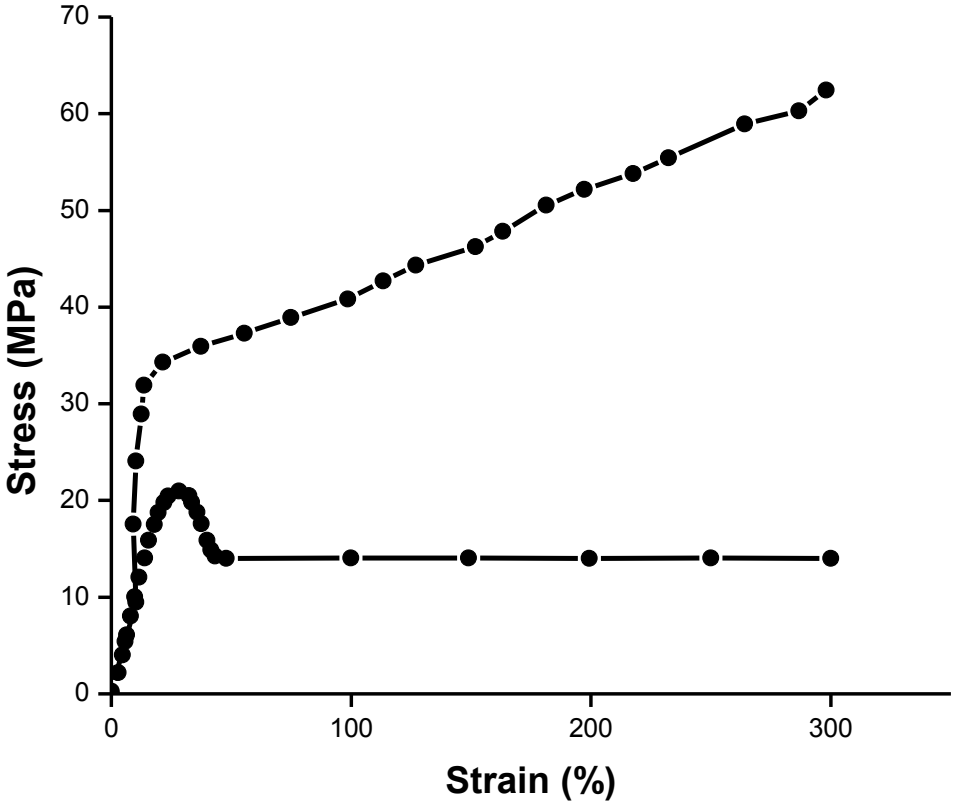

Fig. 4.3 Representative stress-strain curve of the HDPE material.

In order to compare with the experimental procedure and research on the twisting effect to the defect initiation in the HDPE layer, the pinch and torsion tests are modeled in two successive steps in the FEM simulation. In the first step, the top indenter vertically pinches on the top surface of the unit cell. This is an axisymmetric problem and the analysis cost is substantially reduced by using axisymmetric elements compared with a fully three-dimensional model. In this simulation, the displacement of the top indenter is 0.018 mm which is $0.9h$. Large deformation (i.e., geometric nonlinearity) is used in the simulation. In the second twisting step, torsion along z axis is not symmetric with z axis (axis of symmetry in pinch test) and thus $\tau_{z\theta}$ is nonzero in the battery. Therefore a full

three-dimensional model is used to simulate the indenter twist in the experiment. The displacement and stress fields result from step one are first imported into the three-dimensional model, and the top indenter is then applied with a maximum rotation angle of 12°. The rigid body motion of the specimen is removed by fixing the transverse translation of the unit cell center line ($u_i = 0, i = 1, 3$). The Coulomb friction model is used between the indenter and the specimen, and the effect of friction coefficient will be studied in details.

Since this paper focus on the initiation of ISCr created by the pinch and torsion tests, the surface interactions within the unit cell are not considered. Therefore, we tie each contact surfaces within the unit cell, i.e. surfaces between the Al and separator layers and surfaces between Cu and separator layers to reduce the computation cost from the contact iterations and numerical divergence in ABAQUS.

4.3. FEM Results and Discussion

4.3.1 Pinch Test

In the pinch and torsion experiments [157], ISCr in the Li-ion battery is intentionally created by breaking the separator layer to trigger the chemical reactions. The open voltage between the anode and the cathode is closely monitored to ensure that the indenter will be retreated immediately whenever a selected voltage drop (e.g. 0.1 V) is measured. The failure of the separator is due to the high tensile strain caused by the contact. To predict the ISCr location, the tensile zone in the separator layer in the unit cell beneath the spherical contact is characterized by the absolute value of maximum principal strain over minimum principal strain, i.e. $|\epsilon_I/\epsilon_{III}|$, and is plotted as a top view in Fig. 4.4a. Experimental research shows that the ductile failure process in HDPE occurs due to the localized necking after excessive elongation at an intermediate strain rate, a typical rate for our pinch-torsion test [153, 158]. When $|\epsilon_I/\epsilon_{III}| > 1$, the location is under tension state where the necking is mostly likely to initiate (denoted as red zones in Fig. 4.4a). The blue zone in Fig. 4a undergoes compressive deformation. It is shown that the

spherical indentation results into a local tension zone in the separator near the indenter but outside the contact area. The inner radius r of the tension zone is about $1.2a$ and the outer radius is approximate $1.8a$ where a is the contact radius. The distribution of the max principal strain ϵ_1 in the separator is shown in Fig. 4.4b. The highest value of max principal strain $|\epsilon_{\mathrm{I}}|_{max}$ in separator layer exists at the point $1.35a$ away from the center and is under tension. This simulation result qualitatively agrees with our experimental examination such that holes on the separators usually appeared at locations some distance away from the center of the impression as shown in Fig. 4.5. After pinch (Fig. 4.5a) and pinch torsion test (Fig. 4.5b), the separators layer in the unit cell are observed with a hole outside the contact area.

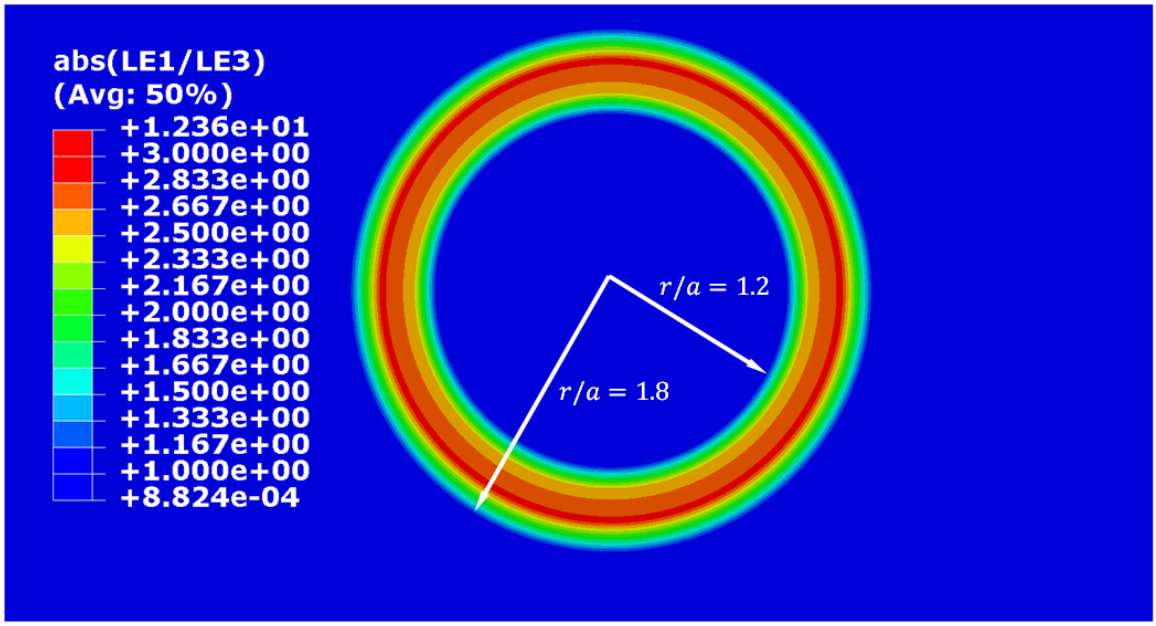

(a)

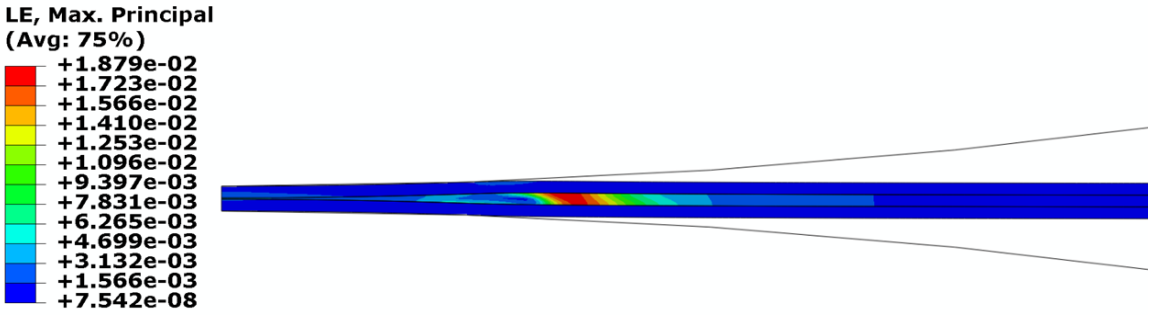

(b)

Fig. 4.4 (a) Top-view contours of absolute value of $\epsilon_I/\epsilon_{III}$ in the separator layer in pinch-only test. The non-blue colors denote the region under tension. (b) Cross section view of the distribution of maximum principal strain ϵ_I after an indentation of 0.018 mm in unit cell.

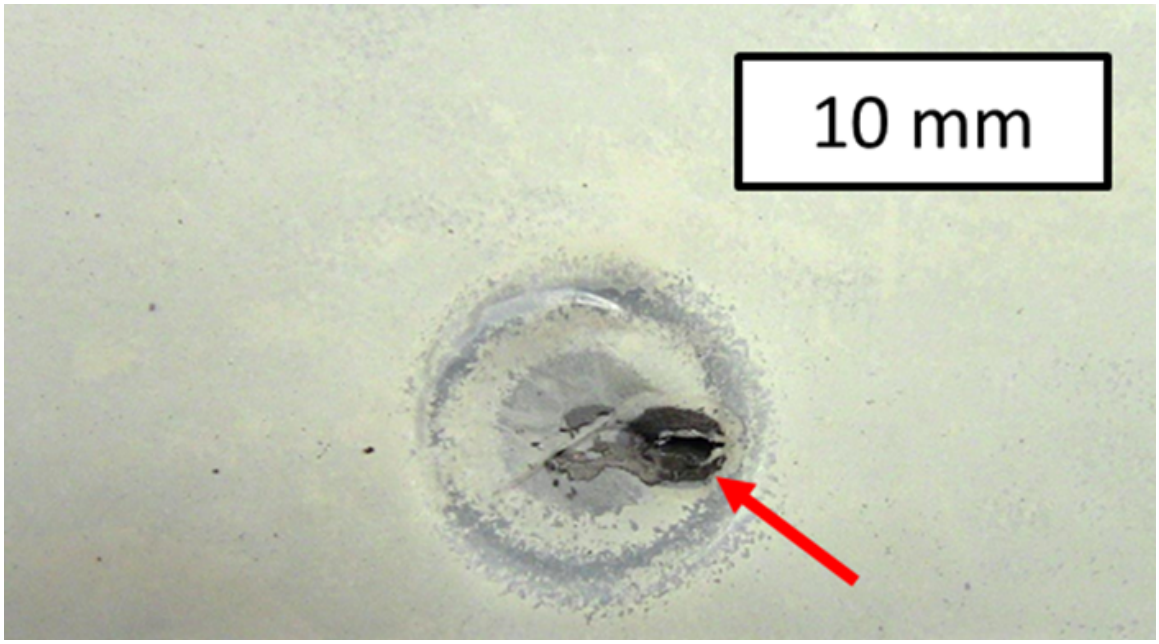

(a)

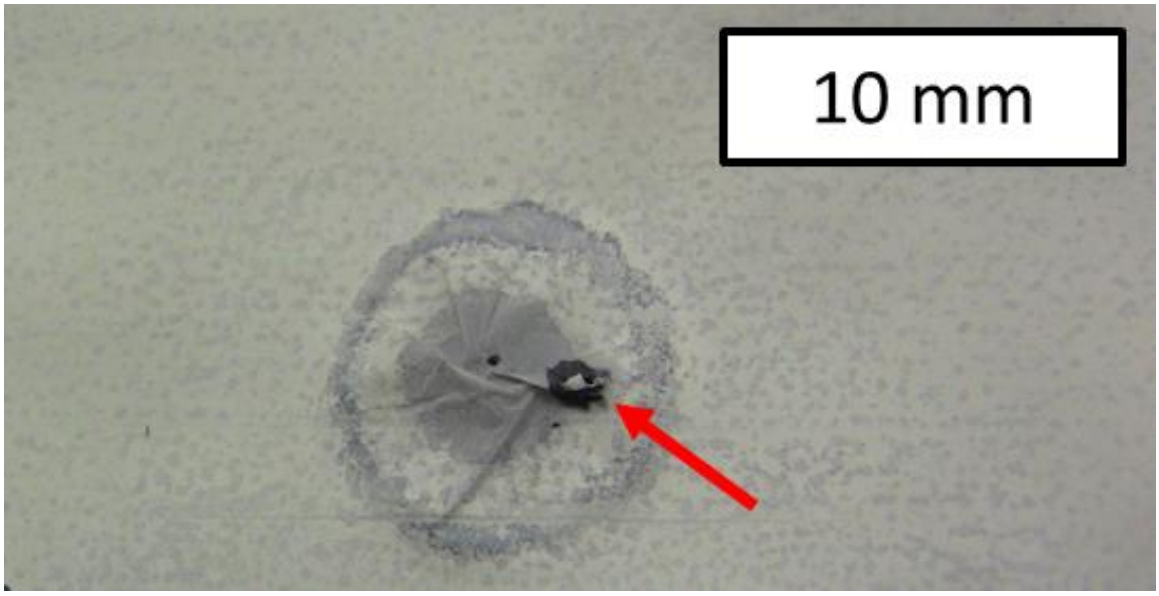

(b)

Fig. 4.5 Optical graphs showing broken separators after (a) a pinch test and (b) a pinch-torsion test. The pointed cracks in the separator layer are initiated outside the spherical contact surface for both tests.

4.3.2 Pinch-Torsion Test

It has been observed in our recently developed pinch-torsion test method [157] that the initial axial load needed to create ISCr in the unit cell drops significantly if a small amount of torsion is applied on the indenter. To investigate the effect of torsional component on initiating defect during pinch test, a full three-dimensional torsion model is simulated. As stated earlier, we first import data from the pure pinch test and then conduct a static analysis by applying a rotation on the indenter. Fig. 4.6 shows the comparison of the strain fields in the separator in top view before (Fig. 4.6a) and after (Fig. 4.6b) the torsion is applied. The friction coefficients between the indenter and the unit cell top and bottom surfaces are chosen to be 0.3. After the torsion, the size of the tension zone is not changed noticeably. However, the maximum principal strain ϵ_I in the tension zone increases significantly (by 77.7%) after the indenter is twisted by 12°. It demonstrates that a slight twisting of the indenter can assist the defect generation which is consistent with our experimental observation [157]. In order to understand the effect of friction coefficient between the contact surfaces, μ, on the pinch and torsion test, the maximum ϵ_I is plotted as a function of θ in Fig. 4.7 for three different friction coefficient values. When a small twist is applied to the indenter, the maximum ϵ_I increases almost linearly with the twist angle. The slope of the maximum ϵ_I and θ curve gradually decrease with increasing twist angle until the maximum ϵ_I reaches a plateau at a twist angle about 5°.

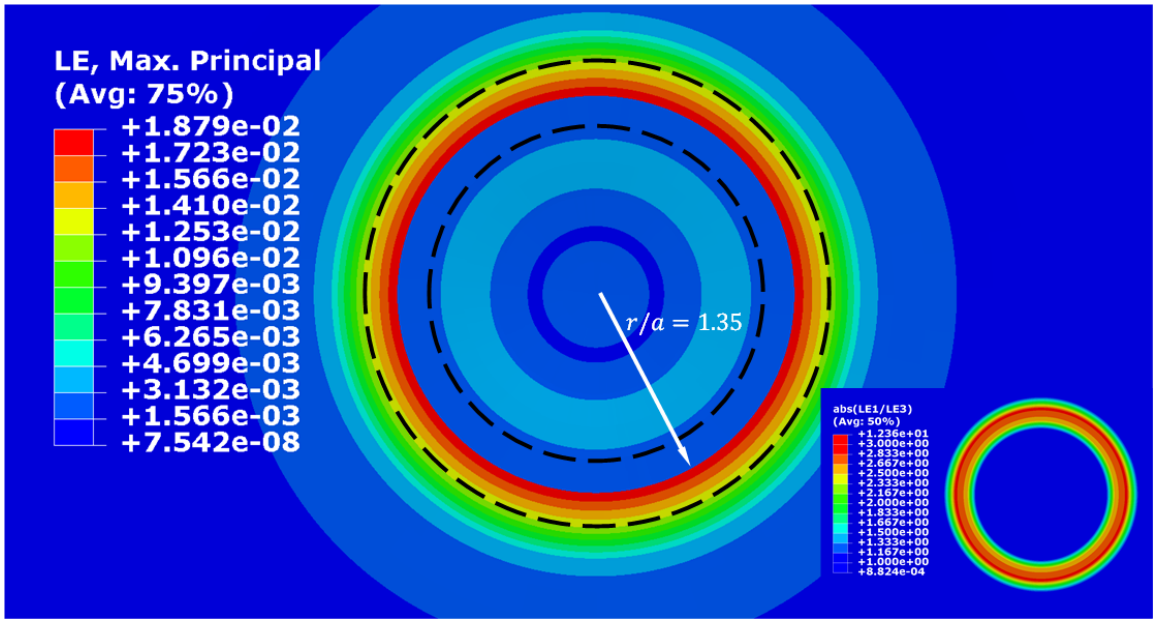

(a)

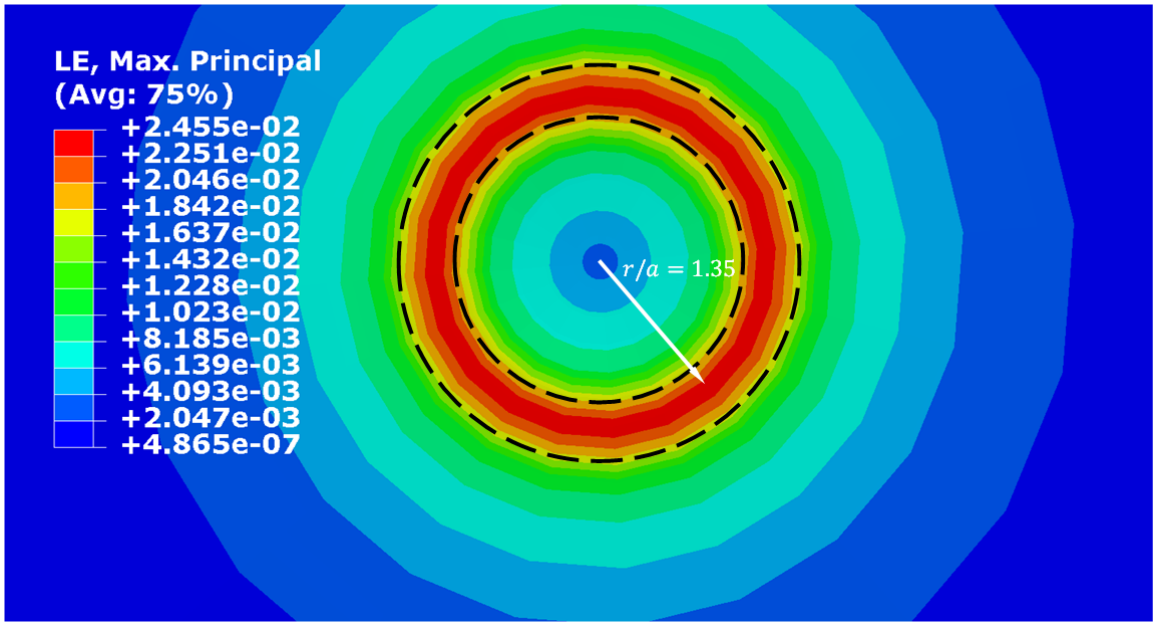

(b)

Fig.4.6. Simulated distribution of ϵ_I in separator layer (a) before twisting (b) after twisting with angle of 12˚. The black dash lines denote the tension zone.

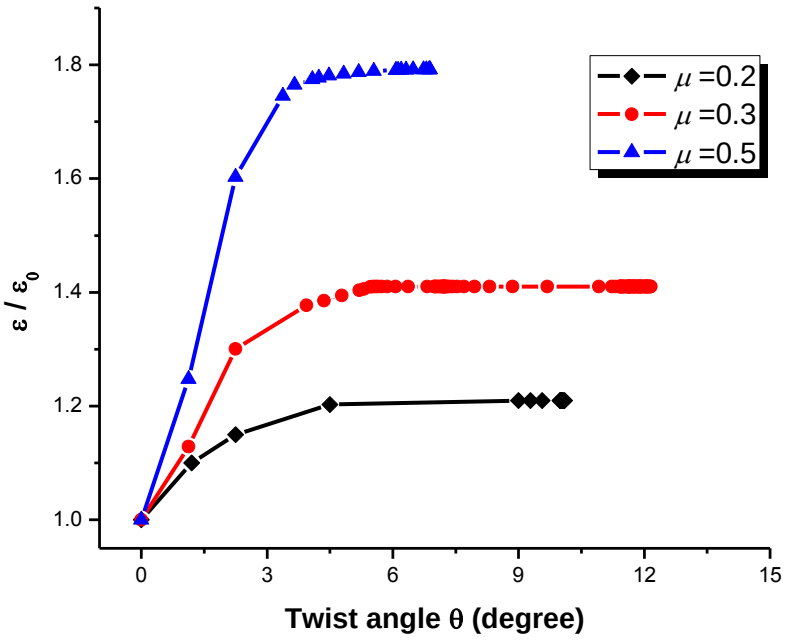

Fig. 4.7. The maximum principal strain ϵ_I as a function of twist angle θ with different friction coefficients μ. The strain ϵ_I during the torsion test is normalized by the maximum principal strain in HDPE when the pinch test ends which has negligible dependence on the friction coefficient.

The above phenomenon can be explained by an elastic contact analysis [16, 159, 160]. For an elastic half-space under spherical contact, the normal contact pressure distribution in the contact area is given by the Hertz theory:

$$p(r) = p_0\sqrt{1-\left(\frac{r}{a}\right)^2} \tag{4-2}$$

where a is the contact radius, $p_0 = \left(\frac{6PE^{*2}}{\pi^3 R^2}\right)^{1/3}$ is the maximum contact pressure and E^* is the reduced modulus[18]. The maximum contact pressure resides on the center of the

contact area and monotonically decreases along the radial direction. If a torque M_z is applied, the tangential traction $q(r)$ in the contact area is distributed as,

$$q(r) = \frac{3M_z r}{4\pi a^3}(a^2 - r^2)^{-0.5} \tag{4-3}$$

where, mathematically, the torsional shear traction goes to infinity at the edge of the contact area (i.e. $r \to a$). Such a solution is similar to the Mode-III crack tip field at the contact edge where the classic inverse-square-root singularity resides, and obviously it holds only when the interface is perfectly bonded. According to the Coulomb friction law, when $|q(r)| \leq \mu|p(r)|$, there is no tangential slip between the two contact surfaces, and when $|q(r)| > \mu|p(r)|$, there will be a relative slip between the indenter and the substrate. The shear stress singularity at the contact edge clearly leads to the stick-slip behavior as shown in Fig. 4.8a. From Eq. (4-3), after a torque $M_z(\theta)$is applied, where θ is the twist angle, the edge of the contact surface will start to slip immediately due to the large tangential traction. However, the rest of the region in the contact area remains bonded, making the indenter contact surface partially slip on the solid. For any point in the contact area which has a distance r to the contact center, the critical twist angle needed to initiate the slide is related to indent pressure as,

$$q(r) = \mu p(r) = \frac{3\mu P}{2\pi a^3}(a^2 - r^2)^{\frac{1}{2}} \tag{4-4}$$

In this study, we assume the static friction coefficient is the same as the kinetic friction coefficient. Therefore, once the two contact surfaces change state from stick to slip, the tangential traction will remain as a constant at the value of maximum static shear force, i.e. $\mu p(r)$. The largest $q(r)$ and thus the largest shear stress $\tau_{z\theta}$ in the contact surface always occurs at the place where it is just start to slip. We denote the distance between the $q(r)$ maxima and the contact center as $c(\theta)$. A representative profile of $q(r/a)$ when the indenter partially slips on the contact surface is plotted in Fig. 4.8a. where $q(r)$ reaches its peak at $c(\theta)$. For location $r > c(\theta)$ in the contact area, it is in

dynamic slipping while location remains static at $r < c(\theta)$. The shear stress $\tau_{z\theta}$ will add a large shear strain $\gamma_{z\theta}$ and thus increase the maximum ϵ_I, corresponding the ascending part in Fig. 4.4. The stick circle eventually shrinks towards the contact center (i.e. $c(\theta) \to 0$) and the free sliding of the indenter is started with a constant moment M_z. Therefore, no further deformation takes place in the battery system and the largest principal strain ϵ_I arrives in the plateau shown in Fig. 4.7.

The above analytic solution is derived from elastic half-spaces. For the thin layer under a pair of spherical contacts, the stick-slip behavior applies qualitatively, but its quantitative feature can only be obtained from finite element analysis. The strain $\epsilon_{z\theta}$ is plotted along the radius at the battery contact surface with twist angles: 2.25° and 7.2° respectively in Fig. 4.8b. For $\theta = 2.25°$, the maximum shear strain appears at $c(\theta) = 0.3a$. For $\theta = 7.2°$, the indenter has fully slipped so that max $\epsilon_{z\theta}$ appears in the vicinity of contact. Based on the analysis above, it is confirmed that torsion of the indenter will increase the intensity of tension inside the sample thus will increase the possibility of breaking the separator layer. However, such effect saturates beyond a critical twist angle and the maximum ϵ_I remains relatively constant, which depends on the friction coefficient μ.

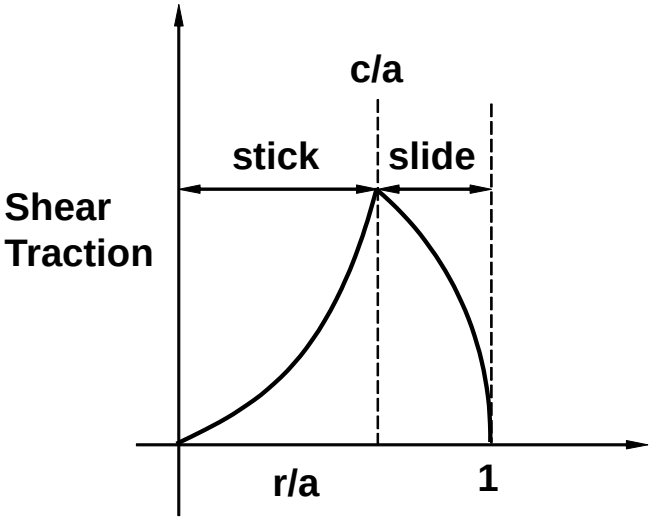

(a)

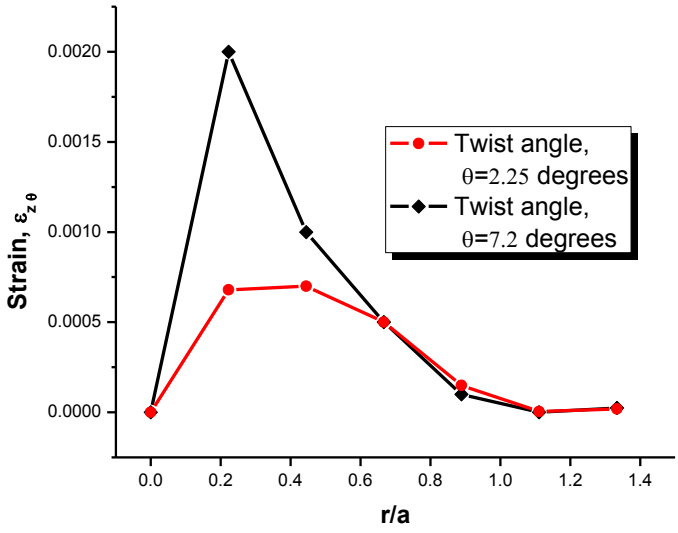

(b)

Fig. 4.8. (a) Shear traction $q(r/a)$ distribution when the indenter is under partial slip. (b) The strain $\epsilon_{z\theta}$ distribution along the radius at the contact surface when θ=2.25˚ and 7.2˚

To explore the maximum ϵ_{I} plateau value in the separator layer, the influence of friction coefficient μ between the surfaces is presented in Fig. 4.9. It shows that the plateau monotonically increases with the increase of friction coefficient μ because from Eq. (4.3), larger friction coefficient will lead to larger tangential stress and thus larger principal tensile strain. In other words, when μ is large, a larger torque is needed to produce a specific twist angle for the indenter, and thus the separator layer will have more severe deformation to assist the defect initiation. In conclusion, torsion component facilitates the failure of the sample by increasing tensile deformation in the polymeric separator.

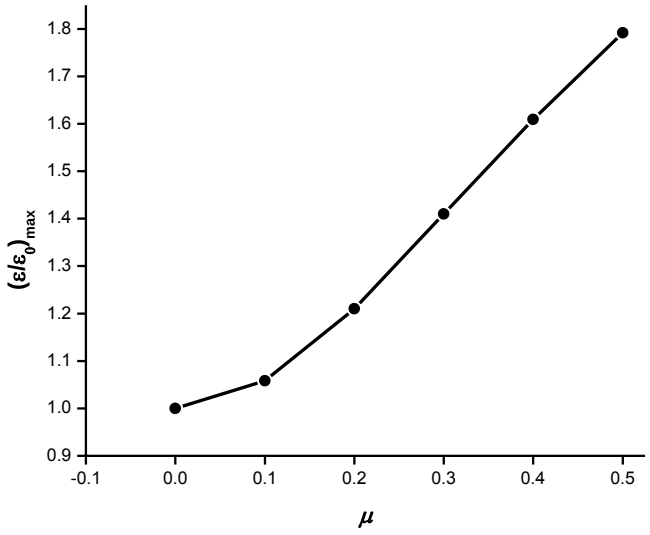

Fig. 4.9. The maximum principal strain ϵ_I after the indenter is twisted with an angle $\theta = 6°$ as a function of friction coefficients μ.

Our recent study compared the pinch and pinch-torsion tests in terms of the axial load needed to induce ISCr. For a three-layer dry cell that had a configuration similar to Fig. 4.2, it was discovered the axial load generating ISCr decreased from approximately

630 N under pure pinch loading to about 400 N under a combined pinch/torsion loading – a reduction of 36.5%. The reduction is explained in Fig. 4.10 where a fix twist angle is applied to different indenter force F and the maximum principle strains in different cases are plotted. We also make a reference case by applying an indentation force F_0 on the unit cell and read the maximum principle strain $\epsilon_0$without any twist to the indenter. Fig. 4.10 shows that after a slight twist angle 2.7˚ is applied, one would need less indentation force (a reduction of 33%) to create same amount of maximum principal strain (i.e. $\varepsilon/\varepsilon_0 = 1$) in the unit cell. It is in line with what is observed in our recent study [11]. On the other hand, it is noticed that at the same applied load, the maximum principle strain inside HDPE increases significantly with θ from 1˚ to 2˚. The coincidence of data for angles larger than 2˚ shows that the indenter is in dynamic slipping already after twisted 2˚ at small applied load level (i.e. F/F_0 is less than 0.9). When indenting with a large load, e.g. $F/F_0 \to 1$, higher twisting angle is needed to make the contacting surfaces fully slip. And the maximum principle strain increases by 17% with the twisting angle θ from 2˚ to 5˚.

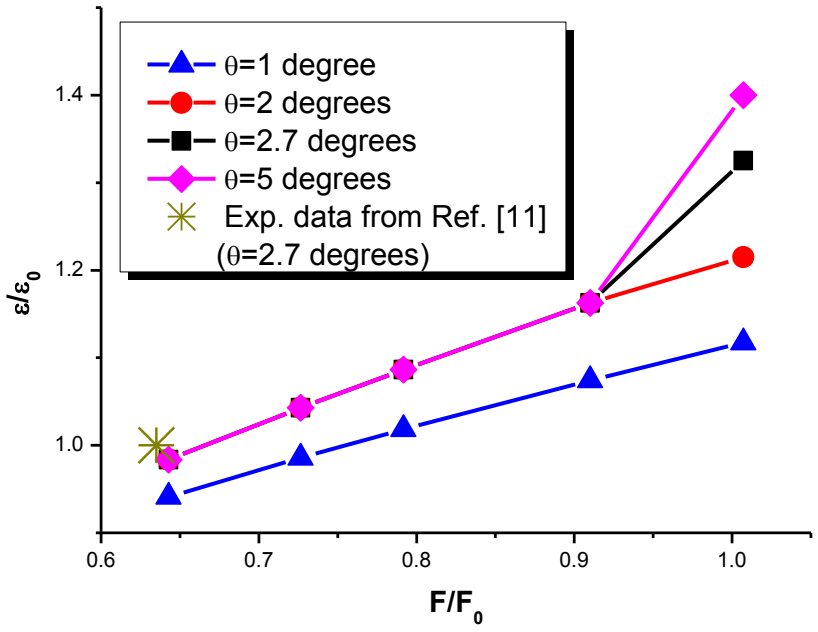

Fig. 4.10. The maximum principal strain ϵ_I as a function of indentation force at different fixed twist angles. F_0 and ϵ_0, respectively, are the indentation force and the maximum principal strain when no twisting is applied. The experimental data point was taken from Ref [157], which represented results from multiple measurements. Since those samples were nominally identical they failed under similar conditions and appeared to be a "single" data point in Fig. 10, which has normalized axes.

4.4. Conclusions

In this paper, finite element analysis is used to simulate deformation of Li-ion battery layers under pinch and pinch-torsion conditions. The simulation discovery is in agreement with our previous experimental results. Several conclusions can be drawn as follows:

1. Spherical indentation delivers tensile zone inside the sample instead on the surface comparing with other experiments such as flat end punch and bending test, making it an attractive method to simulate ISCr in Li-ion batteries.

2. A slight twist of the indenter introduces the shear strain, which increases the maximum principal strain in tension zone and thus facilitates the failure of the polymer. During this stage, the indenter and the contact surface partially slip with co-existence of a slip region and a stick region.

3. Beyond a critical angle, the indenter is free to spin relative to the battery and the maximum principal strain ϵ_I takes its limit value, which highly depends on the friction coefficient μ. Therefore, controlling surface condition on the indenter or battery surface could be utilized to control ISCr events.

Chapter 5 Future works and perspectives

Although many insightful results are obtained in this dissertation, these works can be further extended along following lines:

1. The yield strength dependence on strain rate can be studied for molybdenum-alloy nanofibers with varying initial dislocation density at different per-strain levels. The result will be expected to be stochastic. This is because the sample size is comparable to the feature sizes of dislocation microstructure. The objective of the work will de-convolute the coupling of the stochastic behavior and strain rate sensitivity. A negative strain rate dependence will be inferred from the yield experiment.

2. In this dissertation and some previous works in our group, the indentation size effect on yielding has been well discussed based on the homogeneous-heterogeneous model. However, these researches are mainly based on the clean crystal. However, the work to discuss the effect of another significant factor, initial defect density, on yielding has not been seen yet. As a result, it is a possible way to conduct nanoindentation experiment for sample with different initial defect density to prove the validity of the statistic model in this dissertation.

3. In this dissertation, the successive pop-in behavior has been discussed in detail for homogeneous dislocation nucleation. It will be expected that multiply successive displacement bursts will also occur at a lower load, much lower than the theoretical strength. At this case, the pop-in mechanism is heterogeneous. The heterogeneous pop-in behavior is highly statistical. We can use the framework of homogeneous-heterogeneous model, which was often used to predict the probability of 1^{st} pop-in event in past, with some fundamental and necessary modifications to the codes, to see how the microstructure evolves during the successive pop-in events and what are the key factors to have the mode of several pop-in events on the load-displacement curve during heterogeneous pop-in.

References

[1] G.E. Dieter, D. Bacon, Mechanical metallurgy, McGraw-Hill New York, 1986.

[2] W.C. Oliver, G.M. Pharr, Journal of Materials Research, 7 (1992) 1564-1583.

[3] W.C. Oliver, G.M. Pharr, Journal of materials research, 19 (2004) 3-20.

[4] F. Fröhlich, P. Grau, W. Grellmann, physica status solidi (a), 42 (1977) 79-89.

[5] S. Bulychev, V. Alekhin, M. Shorshorov, A. Ternovskii, G. Shnyrev, Ind. Lab., 41 (1975) 1409-1412.

[6] J. Field, M. Swain, Journal of Materials Research, 8 (1993) 297-306.

[7] J. Hay, G. Pharr, Materials Park, OH: ASM International, 2000., (2000) 232-243.

[8] T.F. Page, W.C. Oliver, C.J. McHargue, Journal of Materials Research, 7 (1992) 450-473.

[9] J. Li, K.J. Van Vliet, T. Zhu, S. Yip, S. Suresh, Nature, 418 (2002) 307-310.

[10] Y. Chiu, A. Ngan, Acta materialia, 50 (2002) 1599-1611.

[11] T. Zhu, J. Li, K. J Van Vliet, S. Ogata, S. Yip, S. Suresh, Journal of the Mechanics and Physics of Solids, 52 (2004) 691-724.

[12] C. Schuh, J. Mason, A. Lund, Nature Materials, 4 (2005) 617-621.

[13] J.K. Mason, A.C. Lund, C.A. Schuh, Physical Review B, 73 (2006) 054102.

[14] H. Bei, Y.F. Gao, S. Shim, E.P. George, G.M. Pharr, Physical Review B, 77 (2008) 060103.

[15] T. Zhu, J. Li, Progress in Materials Science, 55 (2010) 710-757.

[16] K.L. Johnson, K.L. Johnson, Contact mechanics, Cambridge university press, 1987.

[17] C.A. Schuh, A.C. Lund, Journal of Materials Research, 19 (2004) 2152-2158.

[18] T. Li, Y. Gao, H. Bei, E.P. George, Journal of the Mechanics and Physics of Solids, 59 (2011) 1147-1162.

[19] W. Li, H. Bei, J. Qu, Y. Gao, Journal of Materials Research, 28 (2013) 1903-1911.

[20] Z. Wang, H. Bei, E.P. George, G.M. Pharr, Scripta Materialia, 65 (2011) 469-472.

[21] L. Wang, H. Bei, T. Li, Y. Gao, E.P. George, T. Nieh, Scripta Materialia, 65 (2011) 179-182.

[22] S. Shim, H. Bei, E.P. George, G.M. Pharr, Scripta Materialia, 59 (2008) 1095-1098.

[23] H. Bei, E.P. George, J.L. Hay, G.M. Pharr, Physical Review Letters, 95 (2005) 045501.

[24] A.M. Minor, S.S. Asif, Z. Shan, E.A. Stach, E. Cyrankowski, T.J. Wyrobek, O.L. Warren, Nature materials, 5 (2006) 697-702.

[25] P. Wo, L. Zuo, A. Ngan, Journal of materials research, 20 (2005) 489-495.

[26] D. Lorenz, A. Zeckzer, U. Hilpert, P. Grau, H. Johansen, H. Leipner, Physical review B, 67 (2003) 172101.

[27] M.M. Biener, J. Biener, A.M. Hodge, A.V. Hamza, Physical Review B, 76 (2007) 165422.

[28] M. Fujikane, M. Leszczyński, S. Nagao, T. Nakayama, S. Yamanaka, K. Niihara, R. Nowak, Journal of Alloys and Compounds, 450 (2008) 405-411.
[29] L. Ma, D.J. Morris, S.L. Jennerjohn, D.F. Bahr, L. Levine, Journal of Materials Research, 24 (2009) 1059-1068.
[30] H. Leipner, D. Lorenz, A. Zeckzer, P. Grau, physica status solidi (a), 183 (2001) R4-R6.
[31] J.R. Morris, H. Bei, G.M. Pharr, E.P. George, Physical review letters, 106 (2011) 165502.
[32] C. Zhu, Z.P. Lu, T.G. Nieh, Acta Materialia, 61 (2013) 2993-3001.
[33] Y.Z. Xia, H. Bei, Y.F. Gao, D. Catoor, E.P. George, Materials Science and Engineering: A, 611 (2014) 177-187.
[34] D. Wu, T.G. Nieh, Materials Science and Engineering: A, 609 (2014) 110-115.
[35] T. Li, H. Bei, J.R. Morris, E.P. George, Y. Gao, Materials Science and Technology, 28 (2012) 1055-1059.
[36] J. Li, MRS bulletin, 32 (2007) 151-159.
[37] C.L. Kelchner, S.J. Plimpton, J.C. Hamilton, Physical Review B, 58 (1998) 11085-11088.
[38] J. Knap, M. Ortiz, Physical Review Letters, 90 (2003) 226102.
[39] J. Li, T. Zhu, S. Yip, K.J. Van Vliet, S. Suresh, Materials Science and Engineering: A, 365 (2004) 25-30.
[40] Y. Lee, J.Y. Park, S.Y. Kim, S. Jun, S. Im, Mechanics of Materials, 37 (2005) 1035-1048.
[41] C. Begau, A. Hartmaier, E.P. George, G.M. Pharr, Acta Materialia, 59 (2011) 934-942.
[42] M.A. Lodes, A. Hartmaier, M. Göken, K. Durst, Acta Materialia, 59 (2011) 4264-4273.
[43] F. Seitz, Physical Review, 79 (1950) 890-891.
[44] N.F. Mott, Proceedings of the Physical Society. Section B, 64 (1951) 729.
[45] Y. Estrin, H.S. Kim, F.R.N. Nabarro, Acta Materialia, 55 (2007) 6401-6407.
[46] J.D. Eshelby, Proceedings of the Royal Society of London. Series A. Mathematical and Physical Sciences, 241 (1957) 376-396.
[47] E. Tal-Gutelmacher, R. Gemma, C.A. Volkert, R. Kirchheim, Scripta Materialia, 63 (2010) 1032-1035.
[48] W.G. Mao, Y.G. Shen, C. Lu, Scripta Materialia, 65 (2011) 127-130.
[49] J.R. Rice, Journal of the Mechanics and Physics of Solids, 40 (1992) 239-271.
[50] J.R. Rice, G.E. Beltz, Journal of the Mechanics and Physics of Solids, 42 (1994) 333-360.
[51] G. Xu, A.S. Argon, Philosophical magazine letters, 80 (2000) 605-611.

[52] Y. Gao, H. Xu, W.C. Oliver, G.M. Pharr, Journal of the Mechanics and Physics of Solids, 56 (2008) 402-416.

[53] J.H. Lee, Y. Gao, International Journal of Solids and Structures, 48 (2011) 1180-1190.

[54] J.P. Hirth, J. Lothe, Theory of Dislocations, Krieger Publishing Company, 1982.

[55] H. Wollenberger, Point defects, Physical metallurgy. 3. ed, 1983.

[56] P. Sudharshan Phani, K.E. Johanns, E.P. George, G.M. Pharr, Journal of Materials Research, 28 (2013) 2728-2739.

[57] M. Shell De Guzman, G. Neubauer, P. Flinn, W.D. Nix, MRS proceedings, Cambridge Univ Press, 1993, pp. 613.

[58] Q. Ma, D.R. Clarke, Journal of Materials Research, 10 (1995) 853-863.

[59] J. Swadener, E. George, G. Pharr, Journal of the Mechanics and Physics of Solids, 50 (2002) 681-694.

[60] K. McElhaney, J. Vlassak, W. Nix, Journal of Materials Research, 13 (1998) 1300-1306.

[61] Y. Liu, A. Ngan, Scripta Materialia, 44 (2001) 237-241.

[62] Z. Zong, J. Lou, O. Adewoye, A. Elmustafa, F. Hammad, W. Soboyejo, Materials Science and Engineering: A, 434 (2006) 178-187.

[63] K. Durst, B. Backes, M. Göken, Scripta Materialia, 52 (2005) 1093-1097.

[64] K. Durst, M. Göken, G.M. Pharr, Journal of Physics D: Applied Physics, 41 (2008) 074005.

[65] G.M. Pharr, E.G. Herbert, Y. Gao, Annual Review of Materials Research, 40 (2010) 271-292.

[66] N. Fleck, J. Hutchinson, Advances in applied mechanics, 33 (1997) 295-361.

[67] N. Fleck, J. Hutchinson, Journal of the Mechanics and Physics of Solids, 49 (2001) 2245-2271.

[68] W.D. Nix, H. Gao, Journal of the Mechanics and Physics of Solids, 46 (1998) 411-425.

[69] H. Gao, Y. Huang, W. Nix, J. Hutchinson, Journal of the Mechanics and Physics of Solids, 47 (1999) 1239-1263.

[70] Y. Huang, H. Gao, W. Nix, J. Hutchinson, Journal of the Mechanics and Physics of Solids, 48 (2000) 99-128.

[71] M.E. Gurtin, Journal of the Mechanics and Physics of Solids, 48 (2000) 989-1036.

[72] M.E. Gurtin, Journal of the Mechanics and Physics of Solids, 50 (2002) 5-32.

[73] Y. Huang, S. Qu, K. Hwang, M. Li, H. Gao, International Journal of Plasticity, 20 (2004) 753-782.

[74] Y. Huang, F. Zhang, K. Hwang, W. Nix, G. Pharr, G. Feng, Journal of the Mechanics and Physics of Solids, 54 (2006) 1668-1686.

[75] P. Gudmundson, Journal of the Mechanics and Physics of Solids, 52 (2004) 1379-1406.

[76] D.M. Dimiduk, M. Koslowski, R. LeSar, Scripta Materialia, 54 (2006) 701-704.

[77] A. Acharya, Journal of the Mechanics and Physics of Solids, 49 (2001) 761-784.

[78] A. Arsenlis, D.M. Parks, Journal of the Mechanics and Physics of Solids, 50 (2002) 1979-2009.

[79] A. Arsenlis, D. M Parks, R. Becker, V. V Bulatov, Journal of the Mechanics and Physics of Solids, 52 (2004) 1213-1246.

[80] M.E. Gurtin, Journal of the Mechanics and Physics of Solids, 54 (2006) 1882-1898.

[81] M.E. Gurtin, L. Anand, Modelling and Simulation in Materials Science and Engineering, 15 (2007) S263.

[82] I. Groma, F. Csikor, M. Zaiser, Acta Materialia, 51 (2003) 1271-1281.

[83] A. El-Azab, Scripta materialia, 54 (2006) 723-727.

[84] E. Bittencourt, A. Needleman, M.E. Gurtin, E. Van der Giessen, Journal of the Mechanics and Physics of Solids, 51 (2003) 281-310.

[85] L. Nicola, A. Bower, K.-S. Kim, A. Needleman, E. Van der Giessen, Journal of the Mechanics and Physics of Solids, 55 (2007) 1120-1144.

[86] J.Q. Broughton, F.F. Abraham, N. Bernstein, E. Kaxiras, Physical Review-Section B-Condensed Matter, 60 (1999) 2391-2403.

[87] W.A. Curtin, R.E. Miller, Modelling and simulation in materials science and engineering, 11 (2003) R33.

[88] J. Nye, Acta metallurgica, 1 (1953) 153-162.

[89] D. Tabor, Clarendon Press, Oxford, 2000.

[90] S. Qu, Y. Huang, G. Pharr, K. Hwang, International Journal of Plasticity, 22 (2006) 1265-1286.

[91] G. Feng, W.D. Nix, Scripta Materialia, 51 (2004) 599-603.

[92] G.M. Pharr, J.H. Strader, W. Oliver, Journal of Materials Research, 24 (2009) 653-666.

[93] K. Durst, O. Franke, A. Böhner, M. Göken, Acta Materialia, 55 (2007) 6825-6833.

[94] M. Rester, C. Motz, R. Pippan, Acta Materialia, 55 (2007) 6427-6435.

[95] M. Rester, C. Motz, R. Pippan, Scripta Materialia, 59 (2008) 742-745.

[96] M. Rester, C. Motz, R. Pippan, Journal of Materials Research, 24 (2009) 647-651.

[97] H. Kreuzer, R. Pippan, Materials Science and Engineering: A, 400 (2005) 460-462.
[98] A. Widjaja, E. Van der Giessen, A. Needleman, Materials Science and Engineering: A, 400 (2005) 456-459.
[99] D. Balint, V. Deshpande, A. Needleman, E. Van der Giessen, Journal of the Mechanics and Physics of Solids, 54 (2006) 2281-2303.
[100] Y. Zhang, Y. Gao, L. Nicola, Journal of the Mechanics and Physics of Solids, 68 (2014) 267-279.
[101] Z. Wang, (2012).
[102] K. Durst, B. Backes, O. Franke, M. Göken, Acta Materialia, 54 (2006) 2547-2555.
[103] R.L. Klueh, A.T. Nelson, Journal of Nuclear Materials, 371 (2007) 37-52.
[104] H.A.t. Abderrahim, P. Kupschus, E. Malambu, P. Benoit, K. Van Tichelen, B. Arien, F. Vermeersch, P. D'hondt, Y. Jongen, S. Ternier, D. Vandeplassche, Nuclear Instruments and Methods in Physics Research Section A: Accelerators, Spectrometers, Detectors and Associated Equipment, 463 (2001) 487-494.
[105] A.J. Bushby, S.G. Roberts, C.D. Hardie, Journal of Materials Research, 27 (2012) 85-90.
[106] N.I. Budylkin, E.G. Mironova, V.M. Chernov, V.A. Krasnoselov, S.I. Porollo, F.A. Garner, Journal of Nuclear Materials, 375 (2008) 359-364.
[107] W.G. Johnston, J.H. Rosolowski, A.M. Turkalo, T. Lauritzen, Journal of Nuclear Materials, 54 (1974) 24-40.
[108] G.R. Odette, M.J. Alinger, B.D. Wirth, Annual Review of Materials Research, 38 (2008) 471-503.
[109] R. Agamennone, W. Blum, C. Gupta, J.K. Chakravartty, Acta Materialia, 54 (2006) 3003-3014.
[110] V.V. Sagaradze, V.M. Nalesnik, S.S. Lapin, V.M. Aliabev, Journal of Nuclear Materials, 202 (1993) 137-144.
[111] G.R. Odette, Journal of Nuclear Materials, 85–86, Part 1 (1979) 533-545.
[112] M.A. Meyers, V.F. Nesterenko, D.J. Benson, B.Y. Cao, Y.B. Xu, Metall and Mat Trans A, 35 (2004) 2575-2586.
[113] P. Olsson, C. Domain, J. Wallenius, Physical Review B, 75 (2007) 014110.
[114] I. Toda-Caraballo, P. Bristowe, C. Capdevila, Acta Materialia, 60 (2012) 1116-1128.
[115] S. Ogata, J. Li, N. Hirosaki, Y. Shibutani, S. Yip, Physical Review B, 70 (2004) 104104.
[116] X. Guo, Y. Xia, Acta Materialia, 59 (2011) 2350-2357.

[117] D. Catoor, Y.F. Gao, J. Geng, M.J.N.V. Prasad, E.G. Herbert, K.S. Kumar, G.M. Pharr, E.P. George, Acta Materialia, 61 (2013) 2953-2965.

[118] J. Kwon, M.C. Brandes, P. Sudharshan Phani, A.P. Pilchak, Y.F. Gao, E.P. George, G.M. Pharr, M.J. Mills, Acta Materialia, 61 (2013) 4743-4756.

[119] R.T. Pascoe, C.W.A. Newey, physica status solidi (b), 29 (1968) 357-366.

[120] J. Koike, R. Ohyama, Acta Materialia, 53 (2005) 1963-1972.

[121] J. Zimmermann, H. Van Swygenhoven, S. Van Petegem, C. Borca, Acta Materialia, 60 (2012) 4614-4622.

[122] J. Zimmermann, H. Van Swygenhoven, C. Marichal, S. Van Petegem, C. Borca, B. Bartova, E. Oveisi, C. Hebert, Acta Materialia, 60 (2012) 4604-4613.

[123] H. Bei, E.P. George, G.M. Pharr, Scripta Materialia, 51 (2004) 875-879.

[124] A. Teklu, H. Ledbetter, S. Kim, L. Boatner, M. McGuire, V. Keppens, Metall and Mat Trans A, 35 (2004) 3149-3154.

[125] H.M. Ledbetter, R.P. Reed, Journal of Physical and Chemical Reference Data, 2 (1973) 531-618.

[126] R.L. Fleischer, Acta Metallurgica, 11 (1963) 203-209.

[127] N.N. Greenwood, A. Earnshaw, Chemistry of the Elements, Elsevier, 1997.

[128] A.M. James, M.P. Lord, VNR index of chemical and physical data, Van Nostrand Reinhold, 1992.

[129] Y.F. Gao, G.M. Pharr, Scripta Materialia, 57 (2007) 13-16.

[130] T. Okamoto, K. Nakajima, Journal of Physics D: Applied Physics, 10 (1977) 2445.

[131] G. Simmons, H. Wang, Massachusetts Institute of Technology, Cambridge, Massachusetts.

[132] I.A. Abrikosov, O. Eriksson, P. Söderlind, H.L. Skriver, B. Johansson, Physical Review B, 51 (1995) 1058-1063.

[133] P. Olsson, I.A. Abrikosov, L. Vitos, J. Wallenius, Journal of Nuclear Materials, 321 (2003) 84-90.

[134] A. Crocker, B. Bilby, Acta Metallurgica, 9 (1961) 678-688.

[135] A. Shibata, T. Furuhara, T. Maki, Acta Materialia, 58 (2010) 3477-3492.

[136] P. Franciosi, Acta Metallurgica, 31 (1983) 1331-1342.

[137] C. Marichal, H. Van Swygenhoven, S. Van Petegem, C. Borca, Scientific reports, 3 (2013).

[138] Y.F. Gao, Z. Suo, Journal of the Mechanics and Physics of Solids, 51 (2003) 147-167.

[139] Y. Huang, A User-material Subroutine Incroporating Single Crystal Plasticity in the ABAQUS Finite Element Program, Harvard Univ., 1991.
[140] D. Peirce, R.J. Asaro, A. Needleman, Acta Metallurgica, 30 (1982) 1087-1119.
[141] A.F. Bower, E. Wininger, Journal of the Mechanics and Physics of Solids, 52 (2004) 1289-1317.
[142] P. Sudharshan Phani, K. Johanns, E.P. George, G.M. Pharr, Acta Materialia, 61 (2013) 2489-2499.
[143] D. Kim, S.-J. Lee, B. De Cooman, Metall and Mat Trans A, 43 (2012) 4967-4983.
[144] J. Li, S. Sarkar, W.T. Cox, T.J. Lenosky, E. Bitzek, Y. Wang, Physical Review B, 84 (2011) 054103.
[145] D. Belov, M.-H. Yang, J Solid State Electrochem, 12 (2008) 885-894.
[146] H. Maleki, J.N. Howard, Journal of Power Sources, 191 (2009) 568-574.
[147] R. Spotnitz, J. Franklin, Journal of Power Sources, 113 (2003) 81-100.
[148] M.-L. Lee, Y.-H. Li, J.-W. Yeh, H.C. Shih, Journal of Power Sources, 214 (2012) 251-257.
[149] J. Pérès, F. Perton, C. Audry, P. Biensan, A. De Guibert, G. Blanc, M. Broussely, Journal of power sources, 97 (2001) 702-710.
[150] W. Cai, H. Wang, H. Maleki, J. Howard, E. Lara-Curzio, Journal of Power Sources, 196 (2011) 7779-7783.
[151] E. Sahraei, R. Hill, T. Wierzbicki, Journal of Power Sources, 201 (2012) 307-321.
[152] Y. Xia, T. Li, F. Ren, Y. Gao, H. Wang, Journal of Power Sources, 265 (2014) 356-362.
[153] K.H. Shim, S.K. Lee, B.S. Kang, S.M. Hwang, Journal of Materials Processing Technology, 155–156 (2004) 1935-1942.
[154] A.F. Bower, Applied mechanics of solids, CRC press, 2011.
[155] D.J. Hughes, A. Mahendrasingam, W.B. Oatway, E.L. Heeley, C. Martin, W. Fuller, Polymer, 38 (1997) 6427-6430.
[156] N. Cárdenas, I. Machado, E. Gonçalves, J Mater Sci, 42 (2007) 6935-6941.
[157] F. Ren, T. Cox, H. Wang, Journal of Power Sources, 249 (2014) 156-162.
[158] Y. Ide, J.L. White, Journal of Applied Polymer Science, 22 (1978) 1061-1079.
[159] E. Dintwa, M. van Zeebroeck, E. Tijskens, H. Ramon, Eur. Phys. J. B, 39 (2004) 77-85.
[160] T. Li, J. Lee, Y. Gao, International Journal of Applied Mechanics, 1 (2009) 515-525.

Vita

Yuzhi Xia was born on Oct 8, 1985 in Suzhou, Jiangsu Province, China. His family was originally from Shaoxing, Zhejiang Province, China, a place famous for its exquisite wine and successful businessmen. He got his Bachelor's degree in 2008, majoring in Engineering Mechanics, from Northeastern University (NEU), Shenyang, China. Then he continued his graduate study at Dalian University of Technology (DLUT) for another three years, and got his Master's degree in 2011, majoring Engineering Mechanics.

He enrolled in the doctoral program in the Department of Materials Science and Engineering at the University of Tennessee, Knoxville in 2011. The Doctor of Philosophy degree was received in December 2014.